RESEARCH ARTICLE SUMMARY

SYSTEMS BIOLOGY

A protein network map of head and neck cancer reveals PIK3CA mutant drug sensitivity

Danielle L. Swaney, Dana J. Ramms, Zhiyong Wang, Jisoo Park, Yusuke Goto, Margaret Soucheray, Neil Bhola, Kyumin Kim, Fan Zheng, Yan Zeng, Michael McGregor, Kari A. Herrington, Rachel O'Keefe, Nan Jin, Nathan K. VanLandingham, Helene Foussard, John Von Dollen, Mehdi Bouhaddou, David Jimenez-Morales, Kirsten Obernier, Jason F. Kreisberg, Minkyu Kim, Daniel E. Johnson, Natalia Jura, Jennifer R. Grandis, J. Silvio Gutkind, Trey Ideker*, Nevan J. Krogan*

INTRODUCTION: Genome-sequencing efforts over the past decade have profiled the genetic landscape of thousands of tumors and solidified the concept of cancer as a highly heterogeneous disease. Evidence from these efforts has revealed that thousands of genes are altered in cancer, presenting a high degree of complexity that can be challenging to translate into a molecular or clinical understanding. For example, head and neck squamous cell carcinoma (HNSCC) is the sixth most common malignancy worldwide and, despite a wealth of data detailing the genetic alterations in this tumor type, few targeted therapies are available. Therefore, HNSCC presents an opportunity to apply network biology approaches to identify new therapeutic targets and further our understanding of existing ones.

RATIONALE: Network biology approaches have been successfully applied to bridge the gap between genetic alterations and clinical outcomes; however, such approaches rely heavily upon existing public databases of molecular interactions. With the growing recognition that molecular interactions can vary substantially across cellular contexts, the generation of networks in a cancer context represents a critical approach to interpreting and predicting cancer biology and its clinical outcomes.

To characterize the protein-protein interaction (PPI) landscape of HNSCC, we selected proteins based on altered molecular pathways identified from The Cancer Genome Atlas analysis of HNSCC tumors. Additional proteins were added based on genes with recurrent point mutations or a previously published association with HNSCC. *PIK3CA* (the gene encoding the alpha catalytic subunit of phosphoinositide 3-kinase) is the most commonly mutated oncogene in HNSCC, and although a few canonical mutations are well studied, there are many noncanonical mutations that are less well understood. We conducted affinity purification–mass spectrometry (AP-MS) analysis across three cell lines for 31 genes frequently altered in HNSCC, as well as 16 *PIK3CA* mutations. Two of the lines were HNSCC cell lines with RNA profiles representative of HNSCC patients, and one was an esophageal, non-tumerogenic cell line.

RESULTS: This network analysis uncovered 771 interactions from cancer and noncancerous cell states including wild-type and mutant protein isoforms. We found that 84% of these interactions had not been previously reported in public databases, providing a rich resource of new interactions with cancer relevance.

The data reveal a previously unidentified association of the fibroblast growth factor receptor (FGFR) tyrosine kinase 3 with Daple, a guanine-nucleotide exchange factor, resulting in activation of Gαi and PAK1/2 to promote cancer cell migration. This signaling pathway and cell migration can be effectively inhibited by FGFR inhibitors.

Furthermore, AP-MS analysis for 16 *PIK3CA* mutations revealed differences in PPIs. *PIK3CA* helical domain mutants, the most common in HNSCC, preferentially interact with the HER3 receptor tyrosine kinase. Analysis of isogenic xenografts in mice revealed that PIK3CA mutant interaction specificity can determine the in vivo response to HER3 inhibitors, with PIK3CA helical domain mutations conferring sensitivity to HER3 inhibitor treatment with CDX3379 and the H1047R kinase domain mutation conferring resistance.

CONCLUSION: We outline a framework for elucidating tumor genetic complexity through multidimensional PPI maps. This framework is applied to enhance our understanding of HNSCC and also breast cancer (see Kim *et al.*, this issue). These works also suggest that a vast network of PPIs are left to be discovered. Such interactions, especially when combined with datatypes in a hierarchical model (see Zheng *et al.*, this issue), can reveal new mechanisms of cancer pathogenesis, instruct the selection of therapeutic targets, and inform which point mutations in the tumor are most likely to respond to treatment. We anticipate that the application of this framework will be valuable to translating genetic alterations into a molecular and clinical understanding of the underlying biology of many diseases. ■

The list of author affiliations is available in the full article online.
*Corresponding author. Email: tideker@ucsd.edu (T.I.); nevan.krogan@ucsf.edu (N.J.K.)
Cite this article as D. L. Swaney *et al.*, *Science* **374**, eabf2911 (2021). DOI: 10.1126/science.abf2911

READ THE FULL ARTICLE AT
https://doi.org/10.1126/science.abf2911

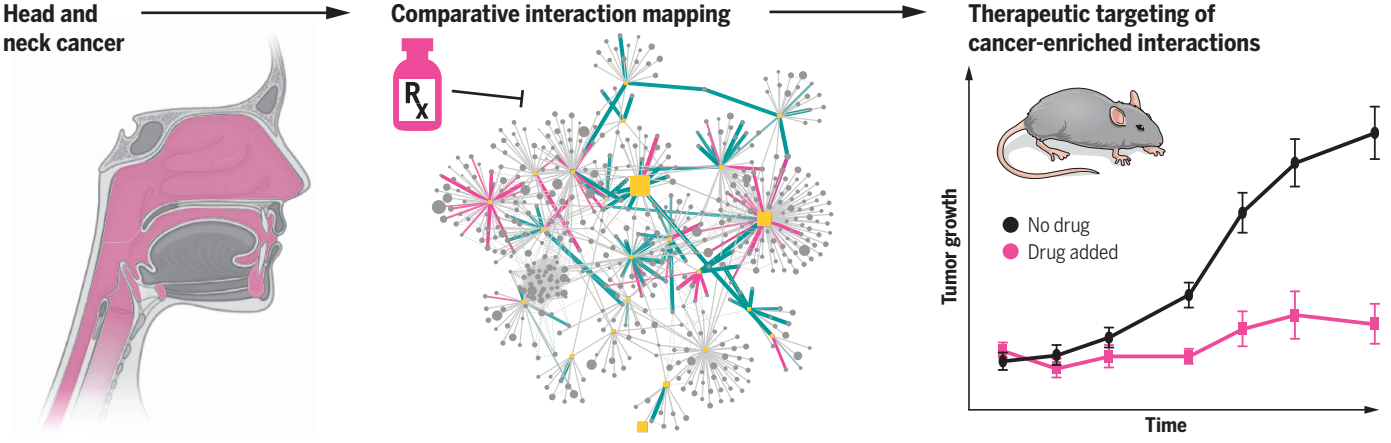

HNSCC interactome analysis. PPI analysis of genes commonly altered in HNSCC reveals interactions that can be therapeutically targeted to inhibit tumor growth.

RESEARCH ARTICLE

SYSTEMS BIOLOGY

A protein network map of head and neck cancer reveals PIK3CA mutant drug sensitivity

Danielle L. Swaney[1,2,3,4], Dana J. Ramms[4,5,6], Zhiyong Wang[4,6], Jisoo Park[4,7], Yusuke Goto[4,6], Margaret Soucheray[1,2,3,4], Neil Bhola[4,8], Kyumin Kim[1,2,3,4], Fan Zheng[4,7], Yan Zeng[4,8], Michael McGregor[1,2,3,4], Kari A. Herrington[9], Rachel O'Keefe[4,8], Nan Jin[4,8], Nathan K. VanLandingham[4,8], Helene Foussard[1,2,3,4], John Von Dollen[1,2,3,4], Mehdi Bouhaddou[1,2,3,4], David Jimenez-Morales[1,2,3,4]†, Kirsten Obernier[1,2,3,4], Jason F. Kreisberg[4,7], Minkyu Kim[1,2,3,4], Daniel E. Johnson[8], Natalia Jura[3,4,10], Jennifer R. Grandis[4,8], J. Silvio Gutkind[4,5,6], Trey Ideker[4,7,11,12]*, Nevan J. Krogan[1,2,3,4]*

We outline a framework for elucidating tumor genetic complexity through multidimensional protein-protein interaction maps and apply it to enhancing our understanding of head and neck squamous cell carcinoma. This network uncovers 771 interactions from cancer and noncancerous cell states, including WT and mutant protein isoforms. Prioritization of cancer-enriched interactions reveals a previously unidentified association of the fibroblast growth factor receptor tyrosine kinase 3 with Daple, a guanine-nucleotide exchange factor, resulting in activation of Gαi- and p21-activated protein kinase 1/2 to promote cancer cell migration. Additionally, we observe mutation-enriched interactions between the human epidermal growth factor receptor 3 (HER3) receptor tyrosine kinase and PIK3CA (the alpha catalytic subunit of phosphatidylinositol 3-kinase) that can inform the response to HER3 inhibition in vivo. We anticipate that the application of this framework will be valuable for translating genetic alterations into a molecular and clinical understanding of the underlying biology of many disease areas.

Genome-sequencing efforts over the past decade have profiled the genetic landscape of thousands of patient tumors and solidified the concept of cancer as a highly heterogeneous disease (*1*–*8*). Evidence from these efforts has also revealed that thousands of genes are altered in cancer, presenting an overwhelming degree of complexity that has limited the power of connecting individual alterations with cancer patient phenotypes. To facilitate interpretation, powerful network biology approaches have been developed in which protein network knowledge is used to aggregate individual tumor mutations and, on the basis of altered networks, to predict patient survival and response to therapy (*9*–*19*). Such network-based approaches rely strongly on existing databases of molecular interactions. To date, publicly available human protein-protein interaction (PPI) networks have been populated primarily by systematic efforts either without human cellular context (yeast two-hybrid) (*20*, *21*) or by affinity purification–mass spectrometry (AP-MS) (*22*–*24*) in workhorse cell lines that lack cancer context, such as human embryonic kidney (HEK) 293T cells. With the growing recognition that such PPIs can vary highly across cellular contexts (*25*), the generation and incorporation of physical and functional networks in a cancer context likely represents a critical component to interpreting and predicting cancer biology and its clinical outcomes (*26*).

To explore the utility of PPI maps generated in a cancer context, we conducted AP-MS experiments to map protein networks in the context of head and neck squamous cell carcinoma (HNSCC) guided by analyses such as that from The Cancer Genome Atlas (TCGA). HNSCC is a cancer affecting squamous mucosal epithelial cells in the oral cavity, pharynx, and larynx, and is estimated to be the sixth most common malignancy worldwide (*27*). Despite a wealth of data detailing the genetic alterations in this tumor type (*7*), only two types of targeted therapies are presently available (*27*). Therefore, HNSCC presents an opportunity to apply emerging quantitative systems approaches to both identify new therapeutic targets and to further our understanding of existing targets such as PIK3CA. *PIK3CA* is the most commonly mutated oncogene in HNSCC and encodes p110alpha (p110α), the catalytic subunit of phosphatidylinositol 3-kinase (PI3K). A hallmark of numerous tumor types, hyperactivation of PI3K can be directly attributed to either amplification or mutation of *PIK3CA* and results in activation of the Akt/mammalian target of rapamycin (mTOR) pathway. Although the function of canonical PIK3CA mutations (e.g., E542K, E545K, and H1047R) is well studied, much remains to be learned about how the numerous noncanonical mutations regulate PIK3CA interactions and function (*28*–*30*). Here, we present a comparative AP-MS analysis across three cell lines for 31 genes frequently altered in HNSCC, including 16 *PIK3CA* mutations.

Mapping of the HNSCC interactome

To characterize the PPI landscape of HNSCC, we selected proteins on the basis of altered molecular pathways identified from the TCGA analysis of HNSCC tumors (Fig. 1A) (*7*). Additional proteins were added based on genes with recurrent point mutations or a previously published association with HNSCC (*31*–*34*). In total, we selected 33 protein baits, of which 31 were experimentally tractable (see the materials and methods and table S1). Ninety-nine percent of HNSCC patients harbor an alteration in one or more of these proteins (Fig. 1A).

For those baits with recurrent point mutations, both the wild-type (WT) and mutant forms of the protein were tagged, purified, and analyzed. Each bait was expressed as a 3xFLAG-tagged protein under the control of a doxycycline-inducible promoter in biological triplicate in three separate cell lines (Fig. 1B). We selected two human papillomavirus (HPV)–negative HNSCC cell lines (SCC-25 and CAL-33) that harbor many genetic alterations present in the HNSCC patient population (Fig. 1A) and that have previously been shown to have RNA profiles highly correlated with those of HNSCC patients (Spearman correlation = 0.66 and 0.69 for CAL-33 and SCC-25, respectively) (*7*, *32*, *34*, *35*). Additionally, an immortalized nontumorigenic cell line, HET-1A, was used from a similar anatomical location (esophagus) for comparison. A previously described AP-MS workflow was then used to identify PPIs from these three cell lines (Fig. 1B) (*36*). We elected to report a conservative and high-confidence PPI (HC-PPI) map by requiring PPIs to pass stringent criteria by two complementary PPI scoring algorithms: SAINTexpress and CompPASS (see the materials and methods) (*22*, *37*, *38*). Using this workflow, a total of 771 HC-PPIs were identified involving 654 proteins (Fig. 1B; fig. S1, A and B; and data S2 and S3), for an average of 25 PPIs per bait gene.

[1]Quantitative Biosciences Institute (QBI), University of California San Francisco, San Francisco, CA, USA. [2]J. David Gladstone Institutes, San Francisco, CA, USA. [3]Department of Cellular and Molecular Pharmacology, University of California San Francisco, San Francisco, CA, USA. [4]The Cancer Cell Map Initiative, San Francisco and La Jolla, CA. [5]Department of Pharmacology, University of California San Diego, La Jolla, CA. [6]Moores Cancer Center, University of California San Diego, La Jolla, CA. [7]Division of Genetics, Department of Medicine, University of California San Diego, La Jolla, CA. [8]Helen Diller Family Comprehensive Cancer Center, University of California San Francisco, San Francisco, CA, USA. [9]Department of Biochemistry and Biophysics Center for Advanced Light Microscopy at UCSF, University of California San Francisco, San Francisco, CA, USA. [10]Cardiovascular Research Institute, University of California San Francisco, San Francisco, CA, USA. [11]Department of Bioengineering, University of California San Diego, La Jolla, CA, USA. [12]Department of Computer Science, University of California San Diego, La Jolla, CA, USA.
***Corresponding author. Email: tideker@ucsd.edu (T.I.); nevan.krogan@ucsf.edu (N.J.K.)**
†Present address: Department of Medicine, Division of Cardiovascular Medicine, Stanford University, Stanford, CA, USA.

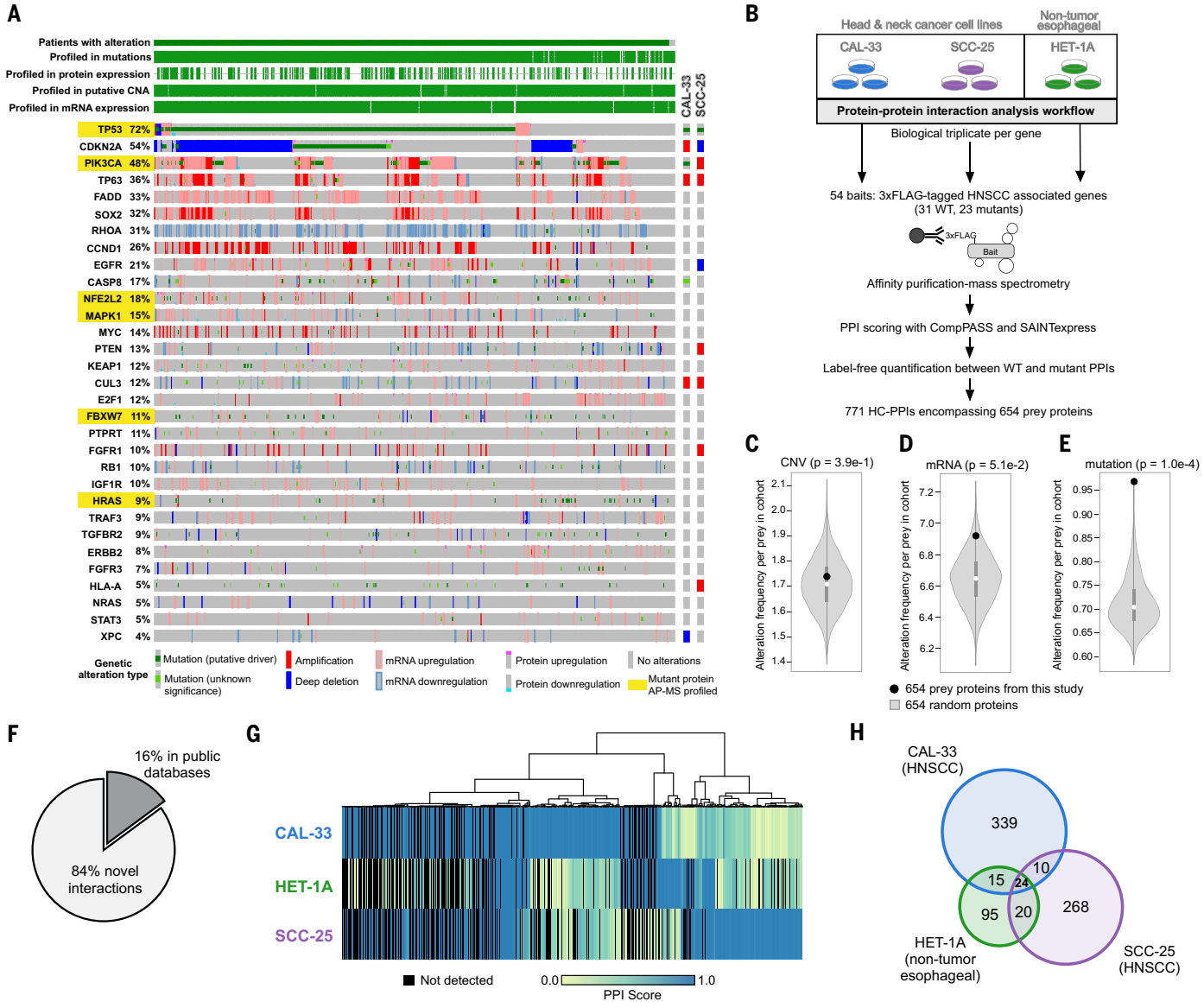

Fig. 1. Experimental design and workflow. (**A**) Alteration frequencies from the HNSCC TCGA provisional dataset (n = 530 patients) for the 31 experimentally tractable genes selected as AP-MS baits in this study. Proteins analyzed in this study are listed, along with the percentage of patients with an alteration in that gene/protein. Each patient is represented by a gray box colored based on the occurrence and type of alteration(s) observed in that patient. Both the WT and mutant protein sequence(s) were analyzed for the genes highlighted in yellow. The genetic alteration types in the two cancer cell lines CAL-33 and SCC-25 are also displayed. (**B**) Experimental workflow in which each bait was expressed in biological triplicate in three cell lines and subjected to AP-MS analysis. (**C** to **E**) Permutation test illustrating the frequency of CNVs (C), mRNA alterations (D), and mutations (E) from randomly selected genes in the HNSCC TCGA data. The white circle indicates the median of the random sampling, and the gray bar represents ±1 SD. The frequency of alterations found in the prey retrieved in this PPI dataset is indicated by the black circle. (**F**) Percentage of HC-PPIs identified in a panel of public PPI databases [CORUM, BioPlex 2.0, or BioGRID low-throughput and multivalidated, and IMEX (*23*, *85*–*87*)]. (**G**) Clustering analysis of all HC-PPIs (n = 771) based on their PPI score, which is an average of the confidence scores reported from SAINTexpress and CompPASS (see the materials and methods for details). A PPI score of 1.0 represents the highest confidence in a PPI. (**H**) Venn diagram illustrating the overlap in HC-PPIs among the three cell lines. For this analysis, only those PPIs passing the HC-PPI filtering criteria by both SAINTexpress and CompPASS were classified as an HC-PPI within an individual cell line.

We and others have shown that alteration profiles in cancer are organized into molecular networks in which the interaction partners of frequently altered proteins incur a higher rate of alteration than a random selection of genes (*9*, *10*, *39*, *40*). Thus, we tested whether our HNSCC HC-PPI set was enriched for different types of alterations measured in the HNSCC TCGA cohort (see the materials and methods). Our dataset was indeed highly enriched for preys with point mutations; however, this enrichment was not observed for alterations in mRNA expression or for chromosomal rearrangements (Fig. 1, C to E). Despite the overall lack of enrichment for generic mRNA alterations, we did find that PPIs from each cell line were significantly enriched in proteins with mRNA expression profiles that were prognostic in TCGA for HNSCC (fig. S1C).

Of the 771 HC-PPIs detected, the majority (84%) had not been previously reported in

public PPI databases (Fig. 1F). This high percentage of new interactions likely reflects the fact that there are differences across cellular contexts for PPIs and that nearly all systematic PPI analyses to date have been performed in only HEK293T or HeLa cell lines (*22*–*24*). This large number of new interactions, presumably due to cell-type specificity, is also supported by the observation that significant differences in PPIs are observed even across the cell lines in this study (Fig. 1G), with only 24 HC-PPIs being conserved across all cell lines analyzed (Fig. 1H and fig. S1D). Many well-studied cancer proteins are included in the new interactions. For example, in SCC-25 cells, we observed physical interactions between the proto-oncoprotein MYC and each of two DNA repair proteins, PARP1 and TOP1. MYC has previously been shown to regulate PARP1 activity (*41*). The MYC:PARP1 interaction is supported by previous studies reporting MYC:TOP1 (*42*) and PARP1:TOP1 interactions (*43*).

Similarly, purification of tagged KEAP1 in SCC-25 cells revealed an interaction with AJUBA, a scaffolding protein involved in the regulation of numerous cellular processes, including negative regulation of Wnt/β-catenin signaling (*44*). Until recently, AJUBA was not associated with HNSCC; however, tumor genome analysis revealed that it is inactivated in 7% of HPV-negative tumors (*7*). The KEAP1:AJUBA interaction was further supported by our identification of a physical connection in HET-1A cells between KEAP1 and SQSTM1, a known AJUBA interactor (*45*–*48*).

A statistical approach to evaluate cell-type specificity of interactions

To identify interactions with relevance to cancer biology, we sought to compare PPIs across cell lines and prioritize those that are seemingly cancer enriched; i.e., those that exist in both CAL-33 and SCC-25, the two HNSCC cancer cell lines, but are absent in the HET-1A nontumorigenic cell line. However, a simple overlap analysis of the sets of HC-PPIs identified by each cell line does not faithfully represent whether a PPI is shared. For example, a PPI might erroneously appear to be specific for a single cell line when it passes the threshold for HC-PPIs in that cell line (i.e., a true positive) while falling slightly below the threshold (i.e., false negative) in a second. Accordingly, we developed a method for calculating differential interaction scores (DISs) for each PPI, with associated Bayesian false discovery rates (BFDRs). This method is based on the SAINTexpress score (*37*), which reports on the probability of a PPI in a single cell line given the AP-MS data. Here, quantitative SAINTexpress probabilities were combined across the three cell lines to generate the DIS (see the materials and methods), allowing for the stratification of PPIs that are enriched in the two cancer cell lines or the noncancerous cells.

Application of the DIS method to our HC-PPIs identified interactions enriched in HNSCC cells as well as those enriched in the HET-1A nontumorigenic background (Fig. 2, A and B, and data S4). For example, the interaction profile for cyclin D1 was substantially rewired between HNSCC and HET-1A (Fig. 2C). Cyclin D1, encoded by the *CCND1* gene, is one of the most commonly altered oncogenes in HNSCC, being amplified in 31% of HPV-negative HNSCC tumors (*7*). Cyclin D1 interacted with the cyclin-dependent kinase inhibitors CDKN1A (p21) and CDKN1B (p27) in all three cell lines, but preferentially interacted with multiple cyclin-dependent kinases (CDKs) only in HNSCC cells. This interaction preference was not unexpected because CCND1:CDK4/6 interactions are known to be essential for cell proliferation and thus can contribute to uncontrolled cell cycle progression in cancer cells (*49*). Consistent with these findings, we observed that the HNSCC cell lines had increased growth rates compared with HET-1A (fig. S2A).

We also found a previously uncharacterized interaction of cyclin D1 with components of the PI3K complex (PIK3CA and PIK3R1/2) exclusively detected by AP-MS in HET-1A cells, an interaction that was further validated by a proximity ligation assay in HET-1A cells expressing FLAG-tagged CCND1 (fig. S2, B to D). Finally, we evaluated the cellular localization of the interaction because cyclin D1 is usually associated with the nucleus, whereas PI3K is primarily associated with the cytoplasm and plasma membrane. We observed the interaction to be 80% cytoplasmic in localization (fig. S2E), indicating a noncanonical localization of cyclin D1, which has been observed previously in certain cell types (*50*). The cell-type enrichment of this particular interaction, along with several others, is further supported by targeted proteomic analysis (fig. S3A).We also evaluated the relationship between cell-type PPI enrichment and both bait and prey expression levels (fig. S3, B to D). In general, we found virtually no correlation between these factors, suggesting that a diversity of factors likely influences PPI cell-type specificity.

Identification of a new FGFR3:Daple interaction that regulates Gαi-mediated migratory signaling

To uncover cancer-enriched interactions, we ranked PPIs by their DIS (Fig. 2D), focusing on those PPIs with greatest enrichment (DIS > 0.5) or depletion (DIS < −0.5) in the HNSCC cell lines (Fig. 2E). This analysis prioritized a previously unknown interaction between fibroblast growth factor receptor 3 (FGFR3) and CCDC88C, which was observed in both CAL-33 and SCC-25 cells but not in HET-1A cells (Fig. 3A). FGFR3 is a receptor tyrosine kinase (RTK) that recognizes FGF and mediates cellular proliferation, survival, and differentiation. CCDC88C, also known as Daple, is a 228-kDa scaffolding protein with roles in mediating both canonical and noncanonical Wnt signaling (*51*–*54*). Daple regulates Wnt through its interaction with the protein Disheveled (Dvl) (*51*) and it can also interact with RTKs, including enhanced growth factor receptor (EGFR) and ERBB2 [also known as human epidermal growth factor receptor 2 (HER2)] (*52*), leading to its phosphorylation and dissociation from Dvl (*52*). Upon this dissociation, Daple translocates from the cytoplasm to the plasma membrane, where it functions as a GEF to activate G proteins (Gαi) and promote Akt signaling, cell migration, and invasion (Fig. 3B) (*55*). We detected the previously characterized ERBB2:Daple interaction (*52*) in CAL-33 cells, in addition to the FGFR3:Daple interaction which we hypothesized may function to promote Gαi activation in an FGFR3-dependent manner.

To test this idea, we used a split luciferase assay (Gαi NanoBiT) in which signal is lost upon activation of Gαi and dissociation from Gβγ (Fig. 3C). As a control, we first transfected an engineered Designer Receptor Exclusively Activated by Designer Drugs (DREADD) receptor and stimulated the resulting cell population with the DREADD ligand clozapine-*N*-oxide (CNO). We observed robust Gαi activation and corresponding loss of luciferase signal in both the CAL-33 and HET-1A cell lines (fig. S4A). Next, we observed that in the CAL-33 cells, where we had detected the interaction between FGFR3 and Daple, FGF stimulation similarly induced Gαi activation; however, no such activation occurred in HET-1A cells (Fig. 3D). Using small interfering RNA (siRNA) knockdowns, we found that Gαi activation in CAL-33 cells was dependent on both FGFR3 and Daple (Fig. 3, D and E, and fig. S4B). FGF also rapidly induced ERK phosphorylation in both CAL-33 and HET-1A cells, consistent with canonical RTK signaling (fig. S4C). FGF-mediated Gαi activation in CAL-33 cells results in downstream phosphorylation of p21-activated protein kinase 1/2 (PAK1/2), an event not observed in HET-1A (Fig. 3F), and this increased phosphorylation was dependent upon both FGFR3 and Daple (fig. S4, D and E). PAK1/2 activity is known to promote cell migration and invasion and is associated with aggressive tumor behavior and poor patient prognosis in HNSCC (*56*). Thus, we also evaluated whether FGF stimulation promoted cell migration, and, indeed, a statistically significant increase was observed (fig. S4, F and G). The FGF-induced migration was not blocked by mitomycin C treatment, suggesting that the effects of FGF promoted cell migration and were independent of growth factor–stimulated proliferation.

Next, we evaluated whether this pathway could be inhibited by the FGFR inhibitor

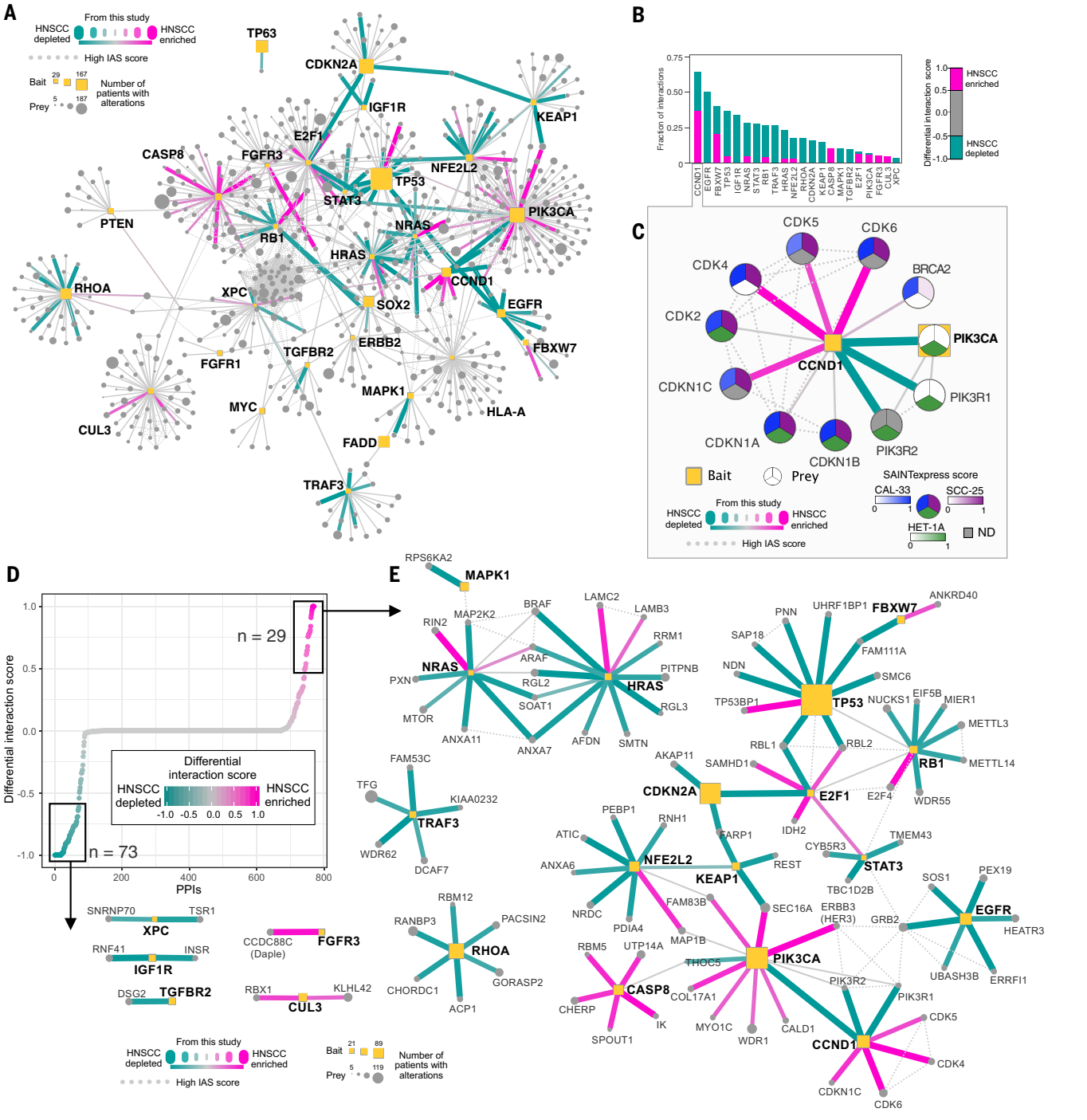

Fig. 2. DIS analysis of the HNSCC-enriched and -depleted interactome. (**A**) Interactome of the union of all HC-PPIs detected across all cell lines. Edges are colored based on their DIS, with pink edges representing PPIs that are enriched in HNSCC (both SCC-25 and CAL-33) compared with HET-1A cells and teal lines representing PPIs that are depleted from HNSCC cell lines. IAS connections represent physical protein-protein association derived from prior studies (*76*) (see the materials and methods). (**B**) For baits with |DIS| > 0.5, the fraction of PPIs for that bait having HNSCC-enriched PPIs with DIS > 0.5, or HNSCC-depleted DIS < −0.5. (**C**) CCND1 interactome. Here, the SAINTexpress score, used for calculation of the DIS, is displayed for each cell line within the prey node. ND, not detected. (**D**) DIS for the entire interactome represented in (A) ranked by DIS. (**E**) Subnetwork of the interactome of the HNSCC-enriched and -depleted interactions.

infigratinib. We found that infigratinib prevented PAK1/2 phosphorylation upon FGF stimulation (Fig. 3G and fig. S4H) and also prevented cell migration (Fig. 3, H and I) in CAL-33 cells. To determine whether these observations may be more broadly applicable in more cell types, we first looked at FGFR3 and Daple expression in all upper airway and esophageal cell lines using DepMap (*57*). We found that both cancer cell lines in which we detected the FGFR3:Daple interaction had above average Daple expression (Fig. 3J). Stratification of cell lines by high and low Daple expression revealed that cell lines with high Daple expression were more sensitive to a pan

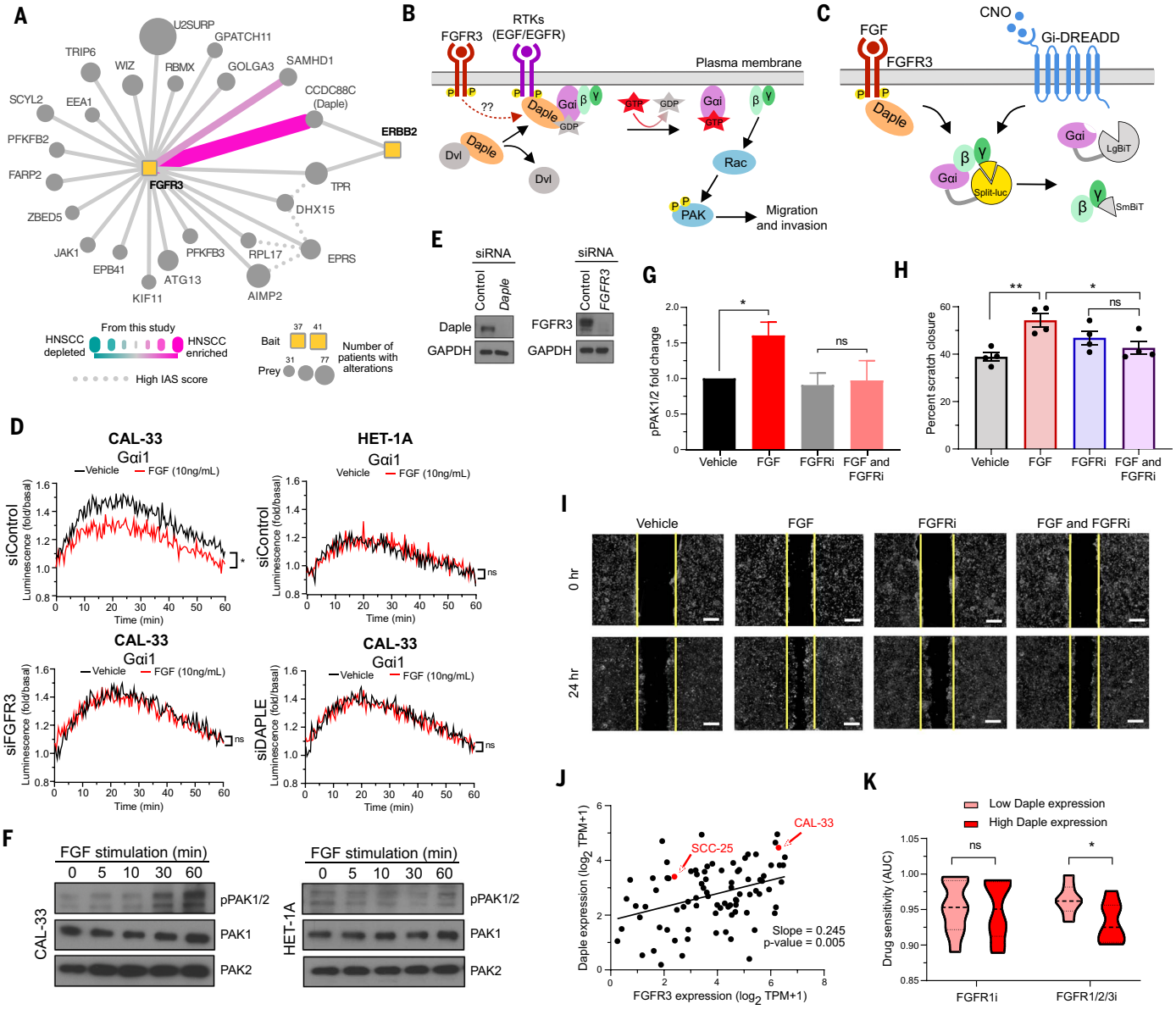

Fig. 3. An HNSCC-enriched FGFR3:Daple interaction mediates activation of cell migratory proteins. (**A**) Differential scoring analysis of the FGFR3 interactome highlighting CCDC88C (Daple) as an HNSCC-enriched interaction partner to both FGFR3 and ERBB2 (HER2). (**B**) Activation of RTKs can disrupt the interaction between Dvl and Daple, allowing Daple to function as a GEF for Gαi. GTP binding causes dissociation of the G protein, leaving Gβγ subunits free to activate migratory signaling through Rac and PAK. (**C**) NanoBiT biosensor measures Gαi activation through dissociation of the luciferase split between Gα and Gβγ. CNO mediates canonical GPCR signaling through the synthetic Gαi-coupled DREADD receptor. FGF mediates HNSCC-specific signaling through FGFR3 and Daple. (**D**) Luminescence measured in CAL-33 and HET-1A cells transfected with Gαi NanoBiT and siRNA (control, FGFR3, or Daple) and stimulated with FGF (10 ng/ml) (*P < 0.05 compared with the vehicle-treated group). (**E**) Immunoblot analysis of CAL-33 cells subject to siRNA knockdown. (**F**) PAK1/2 autophosphorylation measured by immunoblot analysis over a time course of FGF stimulation (0, 5, 10, 30, and 60 min) in CAL-33 and HET-1A cells. (**G**) PAK1/2 autophosphorylation measured by immunoblot analysis in CAL-33 cells stimulated with FGF (10 ng/ml) and/or treated with a 0.5 μM concentration of the pan FGFR inhibitor infigratinib (*P < 0.05 compared with the vehicle-treated group). (**H** and **I**) A vertical scratch was introduced to fibronectin-plated CAL-33 cells and cells were stimulated with FGF (10 ng/ml) and/or treated with 0.5 μM infigratinib. Replicate scratch closures were quantified [*P < 0.05, **P < 0.01 compared with the vehicle-treated group; (H)] and images were taken 0 and 24 hours after FGF stimulation (I). Scale bar, 250 μm. (**J**) Daple and FGFR3 expression plotted for all upper airway and esophageal cell lines in DepMap (*57*), with the two cancer cell lines used in this study highlighted in red. (**K**) Sensitivity of cell lines with high or low Daple expression to either a FGFR1 inhibitor (sorafinib) or a FGFR1/2/3 inhibitor (AZD4547) as quantified by area under the curve (AUC) (*P < 0.05). Cell lines were selected from (J), and for those with corresponding drug sensitivity data, the top five Daple-expressing cells (High Daple) or the bottom five Daple-expressing cells (Low Daple) were used.

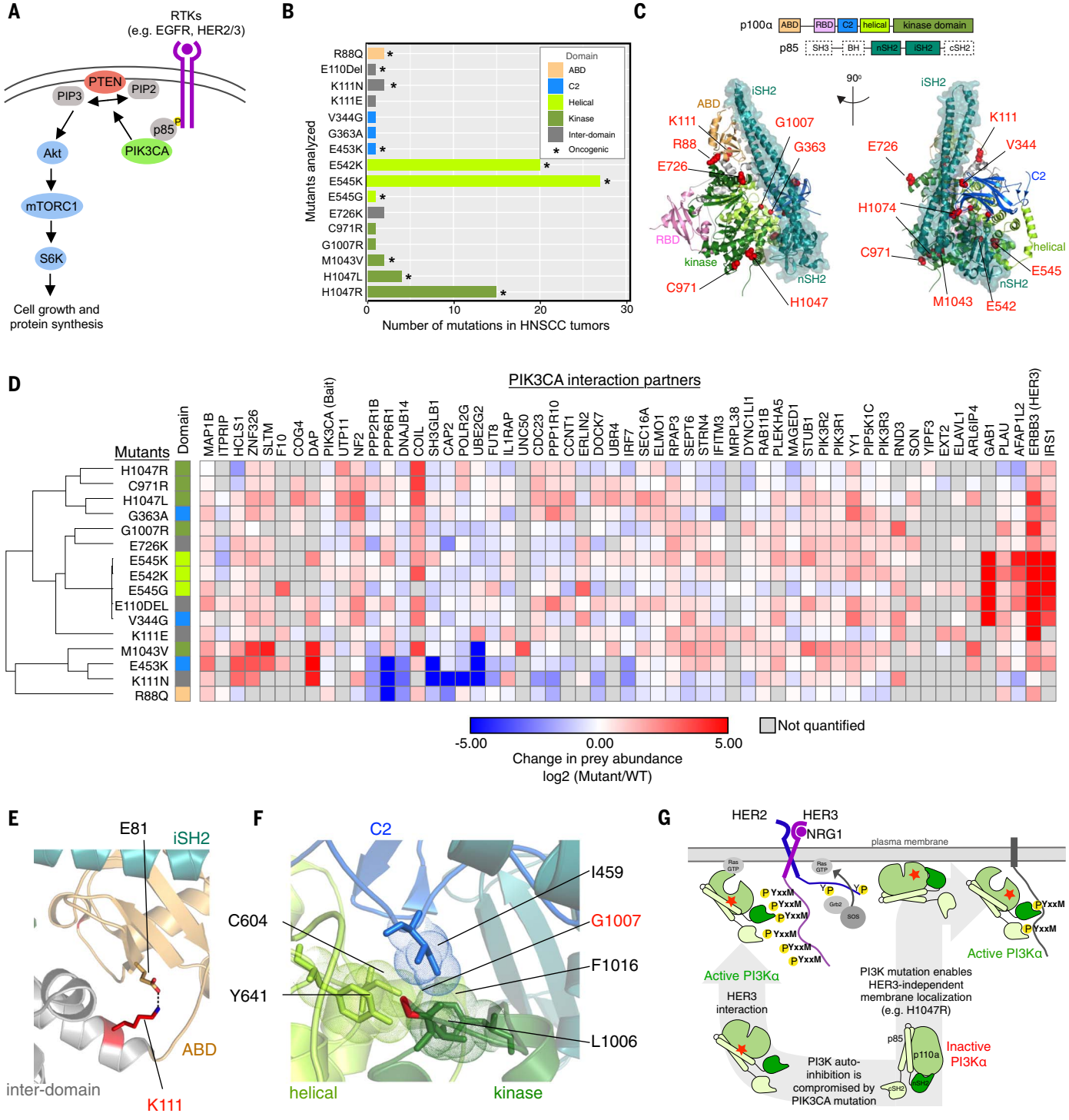

Fig. 4. PIK3CA mutant interactome. (**A**) Overview of the PIK3CA-signaling pathway, which is often stimulated by RTKs that interact with PIK3CA to stimulate RAS/Raf– or Akt/mTORC1–mediated downstream signaling. (**B**) Analyzed *PIK3CA* mutants and their frequency in HNSCC tumors from TCGA. Asterisk (*) denotes mutations annotated as oncogenic in OncoKB (*88*). Graph bars corresponding to each mutation are color coded to indicate their localization within the p110α domain (as indicated in the legend in the top right corner). (**C**) Selected PIK3CA mutations were mapped on the structure of PI3K [Protein Data Bank (PDB) identifier: 4L23] (*89*) by highlighting the mutated residues as red spheres. (**D**) Quantification of PPIs for all PIK3CA HC-PPIs detected in the SCC-25 cell line (all cell lines are displayed in fig. S5). (**E**) Diagram of a magnified view of PI3K illustrating a salt bridge formed between K11 and E81 (PDB: 4L23). (**F**) Magnified view depicting interactions made by G1007 in PI3K (PDB: 4L23). (**G**) Diagram of different mutation-induced PI3K activation mechanisms and their respective HER3-binding preferences.

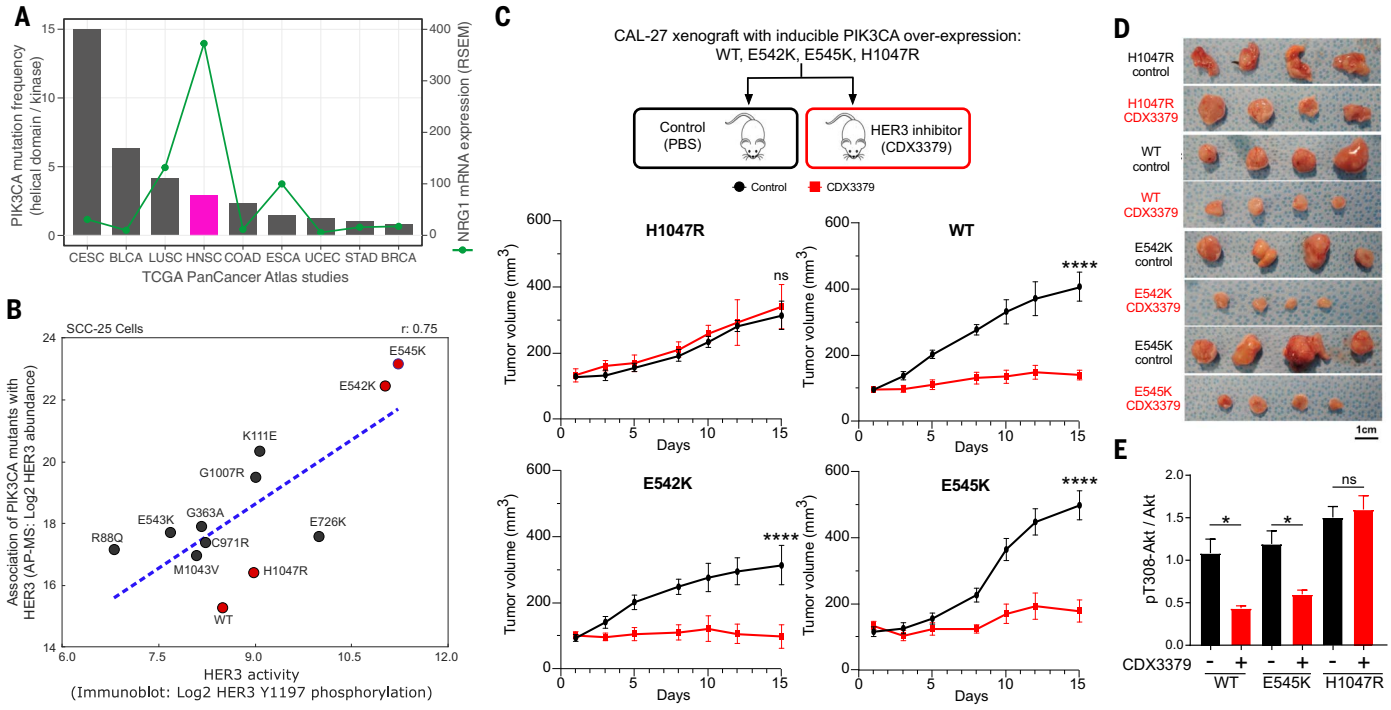

Fig. 5. In vivo targeting of HER3 in the context of different PIK3CA mutants. (**A**) Bar chart representing the ratio of helical domain (E545 and E542) mutations compared with kinase domain mutations (H1047) across TCGA PanCancer Altas studies represented in cBioPortal (*90*). Line graph shows the mRNA expression (RSEM) for NRG1 across the same studies. (**B**) Correlation of Log2 HER3 interaction levels from AP-MS experiments and Log2 HER3 Y1197 phosphorylation levels from immunoblot analysis. All values are normalized by FLAG-PIK3CA levels in their respective experiments. Mutations marked in red were selected for in vivo experiments. (**C** and **D**) CAL-27 cells expressing inducible PIK3CA variants were transplanted into athymic nude mice. Mice were fed with doxycycline to induce PIK3CA expression. When tumor volumes reached ~100 mm^3, mice were treated with vehicle (PBS) or CDX3379 (10 mg/kg, twice a week) for ~15 days, as indicated. Shown are tumor growth curves (C) and representative tumor images (D), (****P < 0.0001 compared with the control-treated group). (**E**) Quantification of immunoblot analysis of signaling events in the same CAL-27 cells in vitro. PIK3CA variant expression was induced by doxycycline (1 μg/ml in culture medium), cells were treated with CDX3379 (1μg/ml for 1 hour), and lysates were analyzed by immunoblotting as indicated. Densitometry analysis of Western blots was performed using ImageJ. Data are represented as mean ± SEM, with n = 3 in each group. (*P < 0.05 compared with the control-treated group).

FGFR inhibitor (FGFR1/2/3) than those with low Daple expression (Fig. 3K). There was no difference in sensitivity to inhibition of FGFR1 among cells with high and low Daple expression, suggesting that the inhibition of FGFR3 may be particularly important for cells with high Daple expression. In total, these results support a mechanism for regulating Gαi activity through FGFR3 and Daple, resulting in increased PAK1/2 activation and cell migration signaling that can be effectively inhibited using FGFR inhibitors.

Quantitative analysis of the mutant PIK3CA interactome

PI3K is a multiprotein kinase complex consisting of a p110alpha (p110α) catalytic subunit that is encoded by the *PIK3CA* gene and a p85-regulatory subunit. Engagement of the SH2 domains of p85 with phosphorylated YxxM motifs is essential for PI3K signaling by releasing p110α autoinhibition and mediating recruitment of PI3K to the plasma membrane (*58*). Upon activation, PI3K becomes a potent mediator of cellular signaling, interacting with both intracellular small GTPases (e.g., RAS proteins) as well as receptor kinases (e.g., EGFR) to regulate downstream signaling primarily through the Akt/mTOR pathway (Fig. 4A). We selected 16 different *PIK3CA* mutations observed in HNSCC patients and quantitatively assessed their effects on p110α interaction partners (Fig. 4B, fig. S5, and data S5). These mutations were distributed across multiple domains within the p110α protein (Fig. 4C).

Examining the PPI profiles of WT PIK3CA and the corresponding mutants in SCC-25 cells revealed a high similarity in interaction patterns for five of the PIK3CA mutants, E110DEL, V344G, E542K, E545G, and E545K (Fig. 4D), driven by a strong increase in interaction of these mutants with three proteins, ERBB3 (HER3), GAB1, and IRS1. All of these prey proteins contain multiple YxxM motifs, representing consensus binding sites for the two SH2 domains (nSH2 and cSH2) located in the PI3K p85-regulatory subunit (*59*). The interaction between phosphorylated tyrosine YxxM motif and the SH2 domain serves to release the PIK3CA autoinhibition and recruit it to the plasma membrane to enable PIP2 phosphorylation. The helical domain mutants (E545K, E545G, and E542K) are poised to disrupt the interaction of p110α with its autoinhibitory p85 subunits, making the p85 nSH2 domain more readily available for interaction with phosphorylated YxxM motifs. Outside of this primary cluster of mutations, we also observed other mutation sites (e.g., K111E and G1007R) with a strong increase in HER3 binding. In these cases also, mutations are expected to compromise the p85-imposed inhibition of the p110α catalytic module, either by disruption of the ABD domain relative to the inhibitory iSH2 module of p85 (K111E; Fig. 4E) or by disruption of a hydrophobic cluster coordinating amino acids from multiple p110α domains (G1007R; Fig. 4F).

HNSCC tumors display a high preference for PIK3CA helical mutations compared with kinase domain mutations (Fig. 5A). Our results suggest that PIK3CA mutations that disrupt the autoinhibition of PI3K (e.g., helical domain mutations) may rely on upstream signals that present multiple phosphorylated YxxM sites for

signaling (Fig. 4G). In HNSCC, this signal is likely to be an activated HER3 receptor. In support of this synergy, HNSCC tumors have the highest mRNA levels for the HER3-activating ligand neuregulin-1 (NRG1) across TCGA PanCancer studies with PIK3CA mutations (Fig. 5A). In vitro analysis of the SCC-25 mutant PIK3CA cell lines also demonstrated a strong positive correlation between the interaction of individual PIK3CA mutants with HER3, as measured by AP-MS, and HER3 activation, as measured by immunoblotting of Y1197 phosphorylation (r = 0.75; Fig. 5B and fig. S6A). Furthermore, the increased interaction between helical domain PIK3CA mutants and HER3 was conserved across several additional cell lines tested (fig. S6, B to D). By contrast, kinase domain mutations are known to innately associate with the membrane and therefore to be less dependent on other proteins for membrane recruitment (*60*). Indeed, we observed low levels of HER3 interaction and phosphorylation (Figs. 4D and 5B and fig. S6, B to D) with the H1047R mutant, suggesting that it might drive oncogenesis in a HER3-independent fashion. We therefore hypothesized that HNSCC tumors harboring *PIK3CA* helical domain mutations may be selectively sensitive to HER3 inhibitor treatment, whereas the kinase domain mutation (H1047R) may confer resistance to HER3 inhibition in vivo.

To test this hypothesis, we generated isogenic CAL-27 cell lines overexpressing WT, E542K, E545K, or H1047R mutant isoforms of PIK3CA. CAL-27 cells were used because they are diploid for WT *PIK3CA*. We injected these engineered lines into the flanks of athymic nude mice (see the materials and methods) and then treated the mice with either saline (control) or the HER3 monoclonal inhibitor CDX3379 over the course of 15 days. Tumor size was monitored, and, as expected, tumors harboring the H1047R mutant were resistant to CDX3379. Unexpectedly, both the helical domain mutants E542K and E545K and WT PIK3CA were sensitive to CDX3379 treatment, resulting in almost complete inhibition of tumor growth (Fig. 5, C and D, and fig. S6E). From these results, we hypothesize that even in the presence of WT PIK3CA, low levels of HER3 binding and HER3 phosphorylation are sufficient and represent an essential mechanism for the recruitment of PIK3CA to the membrane and subsequent PI3K activation. These results underscore that only HNSCC patients carrying *PIK3CA* variants that are still dependent on association with HER3 (WT and helical domain mutants) will likely benefit from HER3-targeted therapeutics.

To further investigate the mechanisms regulating these in vivo phenotypes, we assessed the levels of phosphorylated Akt, a downstream mediator of PI3K signaling, in CAL-27 cells. For mutants in which CDX3379 treatment inhibited tumor growth in vivo, in vitro treatment resulted in significant down-regulation of phosphorylated Akt levels, whereas no such decrease was observed for the CDX3379-resistant H1047R-expressing cells (Fig. 5E and fig. S6F).

Discussion

To truly understand the complexities of the cell, it has been hypothesized that one would need a list of the protein machines, or complexes, that perform all of its functions (*61*). Obtaining such a map would be instrumental, not only for understanding how a healthy cell functions, but also for understanding how mutations affect these machines and the pathways in which they function (*62*) in disease states such as cancer. Using this premise as a motivation, in this study, we examined the physical landscape of PPIs targeting genes genetically linked to HNSCC, revealing hundreds of new PPIs. We observed that these interactions were highly specific to the cell line of study and that mutations in key cancer genes affected PPI interactions in ways that can provide important mechanistic insight and inform response to targeted treatments. In support of previous observations (*25*) and our accompanying manuscript (*63*), these results suggest the exciting premise that there remains a vast network of PPIs left to discover beyond the thousands annotated from HEK293T and HeLa cells (*22*–*24*). We anticipate that developments in high-throughput protein complex determination, such as coelution (*64*), proximity labeling (*65*, *66*), and cross-linking MS (*67*), will enable the rapid advancement of systematic PPI mapping in a diverse array of cancer cell contexts.

An important goal of cancer therapy is to identify drug targets that are applicable across many patients and that achieve high specificity for cancer cells among a heterogeneous tumor cell population. In the context of PPIs, this goal requires moving beyond simply cataloging PPIs toward robust comparative analysis of PPIs across cellular contexts. For this purpose, we have created and demonstrated the value of a DIS to statistically compare PPIs across contexts, which will aid in understanding the underlying biology behind, not just HNSCC but also that of other cancers and disease in general, as evidenced by our application of this approach for breast cancer (*63*). Although the DIS revealed a subset of interactions to be cancer enriched in the three cell lines used in our study, future analysis in additional cell lines would be beneficial to further support these observations.

One interaction uncovered by our DIS approach was a connection between the FGFR3 receptor tyrosine kinase and the GEF Daple, which was seen exclusively in the cancer cell lines. Our findings build upon previous work by demonstrating that FGF stimulation can activate Gαi in a Daple- and FGFR3-dependent manner, which results in activation of PAK1/2 kinases and cell motility. PAK1 expression is highly correlated with aggressive tumor behavior and poor patient prognosis in HNSCC (*56*, *68*). Our work becomes increasingly important as FGFR inhibitors progress toward the clinical setting. Phase II clinical trials with rogaratinib, an FGFR inhibitor, are underway for HNSCC patients with FGFR1/2/3 mRNA overexpression (www.clinicaltrials.gov NCT03088059) after phase I trials demonstrated a 67% objective response rate for solid tumors with FGFR mRNA overexpression (*69*). Additionally, a complete response was observed in a metastatic HNSCC tumor with multiple FGFR amplifications, including FGFR3, when treated with a pan-FGFR inhibitor (*70*). Further work may determine whether the FGFR3:Daple interaction results in frequent coupling of FGFR and PAK1/2 activity in HNSCC patients and if other cancer types also exploit this signaling mechanism. More direct studies are necessary to determine the extent to which FGFR and PAK1/2 activity contribute to clinical outcomes, and PAK1/2 activity could serve as an additional biomarker of patients benefiting from FGFR-targeted therapy.

Our results pertaining to PIK3CA also highlight that oncogenic mechanisms of individual mutations in cancer genes can be reflected in their differences in the corresponding PPIs and that these differences can be exploited for therapeutic benefit. We postulate that the mechanism for the selectivity that we uncovered using PIK3CA mutants lies in the dependence on HER3 signaling that the helical domain mutations maintain. These features of PI3K mutants seemingly contradict previous studies showing that addition of the phosphorylated YxxM motif–containing peptides increases the in vitro catalytic activity of the H1047R mutant but not that of the helical domain mutants (*71*). However, we hypothesize that phosphorylated RTK tails are necessary, not for activation of the helical domain PI3K mutants, but for their recruitment to the plasma membrane, where they need to interact with RasGTP for full activation (*60*). This strong dependence renders cells with such mutations sensitive to HER3 inhibition. We also identified a number of other PI3K mutants that share HER3-binding features with the helical domain mutants, and we predict that their oncogenic potential will also be HER3 dependent (Fig. 4G). Our data also indicate that upstream PI3K activators with a high density of tyrosine phosphorylation sites, represented by the YxxM consensus motifs, such as HER3 and IRS1/2, will be particularly efficient in synergizing with the PI3K helical domain mutants.

Clinical inhibition of HER3 in HNSCC patients is currently being pursued in phase II clinical trials with the monoclonal antibody CDX3379 (www.clinicaltrials.gov identifier NCT03254927) (72). This drug locks the HER3 extracellular domain in an inactive configuration (73) and prevents not only dimerization with coactivating RTKs (e.g., HER2) but also activation of HER3 by neuregulins (e.g., NRG1). These properties make HER3 a particularly promising target because NRG1 is expressed at higher levels in HNSCC than in any other tumor type (74). The results presented here further suggest that HER3 inhibitors present an opportunity to potently target specific *PIK3CA* mutant tumors, a utility that has not been evaluated previously. This is important because *PIK3CA* is one of the most commonly mutated oncogenes in HNSCC (7), but direct targeting of PIK3CA in the clinical setting has been limited by toxicity (75), likely because of its pleiotropic roles in cancer and maintenance of normal cell states. In light of our findings, patient preselection, such as exclusion of PIK3CA H1047R mutation carriers and inclusion of those harboring helical domain mutants, may be a valuable consideration as future phases of clinical trials proceed.

In summary, this study and the accompanying papers in this issue (63, 76) outline a framework for elucidating genetic complexity through multidimensional maps of cancer cell biology. They also demonstrate that such maps can reveal mechanisms of cancer pathogenesis, instruct the selection of therapeutic targets, and inform which point mutations in the tumor are most likely to respond to treatment (26, 77). Therefore, we anticipate that the generation and incorporation of cancer-specific physical and functional networks may represent a critical component to interpret and predict cancer biology and its clinical outcomes. Finally, the framework described here applies not only to cancer but also to many other genetically defined disease areas as well.

Materials and Methods

Reagents and resources

Catalog numbers for all key reagents and resources are listed in table S8.

Bait cloning

Baits were cloned using the Gateway Cloning System (Life Technologies) into a doxycycline-inducible N-term or C-term 3xFLAG-Tagged vector modified to be Gateway compatible from the pLVX-Puro vector (Clontech) by the Krogan laboratory (see data S6). Point mutant baits were cloned through site-directed mutagenesis. All expression vectors were sequence validated (Genewiz).

Cell culture, lentivirus production, and stable cell line generation

HEK293T (ATCC, CRL-3216) and CAL-33 were maintained in Dulbecco's modified Eagle's medium (DMEM; Corning) supplemented with 10% fetal bovine serum (FBS; Invitrogen) and 1% penicillin-streptomycin (Corning). HET-1A was maintained in broncho-epithelial cell grown medium (Lonza), consisting of broncho-epithelial basal medium with the additives of the Bullet kit except GA-1000 (gentamycin-amphotericin B mix). SCC-25 was maintained in DMEM/F12 (Corning) with 10% FBS (Invitrogen), 1% penicillin-streptomycin (Corning), and 400 ng/ml hydrocortisone (Sigma-Aldrich). HET-1A cells were obtained from American Type Culture Collection and SCC-25 was obtained from Thomas Carey (University of Michigan). CAL-33 cells were provided by G. Milano (University of Nice, Nice, France). All cells were maintained in a humidified 37°C incubator with 5% CO_2. Stably transduced HET-1A, SCC-25, and CAL-33 cell lines were maintained in puromycin (2, 2.5, and 0.7 μg/ml, respectively). Bait expression was induced by 1 μg/ml doxycycline for 40 hours. All cell lines were authenticated by the University of California–Berkeley Cell Culture Facility.

Lentivirus was produced for each bait by packaging 5 μg bait vector, 3.33 μg of Gag-Pol-Tat-Rev packaging vector (pJH045 from J. Hultquist), 1.66 μg of VSV-G packaging vector (pJH046 from J. Hultquist) with 30 μl of PolyJet (SignaGen). After incubating at room temperature for 25 min, DNA complexes were added dropwise to HEK293T cells (15-cm plate, ~80% confluency). Lentivirus-containing supernatant was collected after 72 hours and filtered through a 0.45-μm polyvinylidene difluoride (PVDF) filter. Lentivirus particles were precipitated with PEG-6000 (8.5% final) and NaCl (0.3 M final) at 4°C for 4 to 8 hours. Particles were pelleted by centrifugation at 2851*g* for 20 min at 4°C and resuspended in Dulbecco's PBS for a final volume of ~800 to 1000 μl. Stable cell lines were generated by transducing a 10-cm plate (~80% confluency) with 200 μl of precipitated lentivirus for 24 hours before selecting with puromycin for a minimum of 2 days.

Affinity purification

One 10-cm plate of cells (~80% confluency) was washed with ice-cold Dulbecco's PBS and lysed with 300 μl of ice-cold lysis buffer containing 50 mM Tris, pH 7.4, 150 mM NaCl, 1 mM EDTA, 0.5% NP40, 1 mM dithiothreitol (DTT), 1× protease inhibitor cocktail (Roche, complete mini-EDTA free), and 125 U of benzonase/ml. Lysates were flash-frozen on dry ice for 5 to 10 min, followed by a 30 to 45 s thaw in 37°C water bath with agitation and rotation at 4°C for 15 min. Lysate was clarified by centrifugation at 13,000*g* for 15 min at 4°C. A 30-μl lysate aliquot was saved for future bicinchoninic acid assay and Western blot.

For FLAG purification, 25 μl of bead slurry (Anti-Flag M2 Magnetic Beads; Sigma-Aldrich) was washed twice with 1 ml of ice-cold wash buffer (50 mM Tris, pH 7.4, 150 mM NaCl, 1 mM EDTA), and all of the remaining lysate was incubated with the anti-FLAG beads at 4°C with rotation for 2 hours. After incubation, flow-through was removed and beads were washed once with 500 μl of wash buffer with 0.05% NP40 and twice with 1 ml of wash buffer (no NP40). Bound proteins were eluted by incubating beads with 15 μl of 100 ug/ml 3xFLAG peptide in 0.05% RapiGest in wash buffer for 15 min at room temperature with shaking. Supernatants were removed and elution was repeated. Eluates were combined and 10 μl of 8 M urea, 250 mM Tris, 5 mM DTT (final concentration ~1.7 M urea, 50 mM Tris, and 1 mM DTT) was added to give a final total volume of ~45 μl. Samples were incubated at 60°C for 15 min and allowed to cool to room temperature. IODO was added to a final concentration of 3 mM and the mixture was incubated at room temperature for 45 min in the dark. DTT was added to a final concentration of 3 mM before adding 1 μg of sequencing-grade trypsin (Promega) and incubating at 37°C overnight. Samples were acidified to 0.5% trifluoroacetic acid (TFA, pH < 2) with 10% TFA stock and incubated for 30 min before desalting on C18 stage tip (Rainin).

MS data acquisition and analysis

For AP-MS experiments, samples were resuspended in 15 μl of MS loading buffer (4% formic acid, 2% acetonitrile) and 2 μl was separated by a reversed-phase gradient over a nanoflow 75-μm internal diameter × 25-cm long picotip column packed with 1.9 μM C18 particles (Dr. Maisch). Peptides were directly injected over the course of a 75-min acquisition into a Q-Exactive Plus mass spectrometer (ThermoFisher Scientific) or over the course of a 90-min acquisition into an Orbitrap Elite mass spectrometer. Raw MS data were searched against the Uniprot canonical isoforms of the human proteome (downloaded 21 March 2018) using the default settings in MaxQuant (version 1.6.2.10), with a match-between-runs enabled (78). Peptides and proteins were filtered to 1% FDR in MaxQuant, and identified proteins were then subjected to PPI scoring. To quantify changes in interactions between WT and mutant baits, we used a label-free quantification approach in which statistical analysis was performed using MSstats (79) from within the artMS Bioconductor R package. All raw data files and search results are available from the Pride partner ProteomeXchange repository under the PXD019469 identifier (80, 81).

Detailed MS acquisition and MaxQuant search parameters are provided in table S7.

Targeted proteomic analysis

Targeted proteomic analysis of AP-MS samples was performed on a Thermo Q-Exactive Plus mass spectrometer using the same high-performance liquid chromatography conditions as described for the original AP-MS experiments. All peptide and fragment ion selection and quantitative data extraction were performed using Skyline (*82*). Quantitative values were then imported into PRISM version 8 software to perform normalization by bait abundance and statistical testing (two-tailed, unpaired *t* test).

PPI scoring

Protein spectral counts as determined by MaxQuant search results were used for PPI confidence scoring by both SAINTexpress (version 3.6.1) (*37*) and CompPASS (version 0.0.0.9000) (*22*, *38*). All PPI scoring was performed separately for each cell line. For SAINTexpress, control samples in which bait protein was not induced by addition of doxycycline were used. For CompPASS, a stats table representing all WT baits was used. After scoring, the CompPASS WD and *Z*-score were normalized within a given bait for each cell line. The total list of candidate PPIs was filtered to those that met the following criteria: SAINTexpress BFDR <0.05, WD percentile by bait ≥0.95, and *Z*score percentile by bait ≥0.95. PPIs passing all three of these criteria were considered to be HC-PPIs. To enable visualization and analysis of PPIs by confidence score among these three criteria, we also calculated a PPI score as follows: [(WD percentile by bait + *Z*-score percentile by bait)/ 2) + (1 − BFDR)]/ 2. This score places both the PPI confidence from SAINTexpress and CompPASS on a 0 to 1 scale, with 1 being the highest confidence, and then takes the weighted average of these confidence scores.

Permutation test

A permutation test was performed in which genes were drawn from the list of all genes detected in the global protein abundance analysis of the parental cell lines. The null distribution of the average number of samples with variation was learned from 10,000 random gene lists of equal size to the set of interacting partners. This permutation test was performed individually for mutations (excluding silent mutations), copy number variations (CNVs), and mRNA expression. The information for observed variation of each gene is collected from the TCGA head and neck cancer cohort (firehose legacy; downloaded from cbioportal.org/datasets).

Differential interaction scoring

To compare PPIs across cell lines, we developed a method for calculating a DIS and a corresponding FDR using AP-MS data across multiple cell lines. This approach uses the SAINTexpress score (*38*), which is the probability of a PPI being bona fide in a single cell line. Here, we let $S_c(b,p)$ be the SAINTexpress score of a specific PPI denoted as (b,p) in a cell line c. Given that PPIs are independent events across different cell lines, we computed the DIS for each PPI (b,p) as the product of the probability of a PPI being present in both cancer cell lines but absent in the HET-1A normal cell line as follows for each PPI:

$$\mathrm{DIScancer}(b,p) = S_{\mathrm{CAL\text{-}33}}(b,p)S_{\mathrm{SCC\text{-}25}}(b,p)[1 - S_{\mathrm{HET\text{-}1A}}(b,p)]$$

This DIS highlights PPIs that are strongly conserved across two cancer cell lines but not shared by the normal cell line. Additionally, we can highlight PPIs that are present in the control HET-1A cell line, but depleted in both cancer cell lines as follows:

$$\mathrm{DIS_{normal}}(b,p) = [1 - S_{\mathrm{CAL\text{-}33}}(b,p)][1 - S_{\mathrm{SCC\text{-}25}}(b,p)]S_{\mathrm{HET\text{-}1A}}(b,p)$$

We further merged these two DIS scores to define a single score for each PPI, where if $\mathrm{DIS_{cancer}} > \mathrm{DIS_{normal}}$, the DIS is assigned a positive (+) sign, whereas if $\mathrm{DIS_{cancer}} < \mathrm{DIS_{normal}}$, the unified DIS is assigned a negative (−) sign. In this way, the DIS for each PPI is represented by a continuum in which negative DIS scores represent PPIs depleted in HNSCC, whereas positive DIS scores represent PPIs enriched in HNSCC. Additionally, for all DISs that we calculated, we also computed the BFDR estimates at all possible thresholds (p^*) as follows:

$$\mathrm{FDR}(p^*) = i,i(1 - \mathrm{DIS}(pi,pj))I\{\mathrm{DIS}(pi,pj) > p^*\}i,jI\{\mathrm{DIS}(pi,pj) > p^*\}$$

where $I\{A\}$ is 1 when A is true and 0 otherwise. Although these scores were used for comparison across three cell lines, it can also be used more simply to compare between any two cell lines. Such a comparison is calculated as follows where $DIS_{\mathrm{LineA/LineB}}$ results in PPIs specific to cell line A have a positive DIS value, whereas PPIs specific to cell line B results in a negative DIS value:

$$\mathrm{DIS_{CAL\text{-}33/HET\text{-}1A}}(p1,p2) = S_{\mathrm{CAL\text{-}33}}[(p1,p2)(1 - S_{\mathrm{HET\text{-}1A}}(p1,p2)] \text{ or}$$

$$\mathrm{DIS_{SCC\text{-}25/HET\text{-}1A}}(p1,p2) = S_{\mathrm{SCC\text{-}25}}[(p1,p2)(1 - S_{\mathrm{HET\text{-}1A}}(p1,p2)] \text{ or}$$

$$\mathrm{DIS_{SCC\text{-}25/CAL\text{-}33}}(p1,p2) = S_{\mathrm{SCC\text{-}25}}[(p1,p2)(1 - S_{\mathrm{CAL\text{-}33}}(p1,p2)].$$

NanoBiT Gαi1 dissociation assay

The NanoBiT G-protein dissociation assay, based on a split-luciferase system, was performed as previously described with some modifications (*83*). All DNA constructs were provided by A. Inoue (Tohoku University, Japan). NanoBiT plasmids (pCAGGS) include Gαi1-LgBiT, Gβ1-native, and SmBiT-Gγ2 (CAAX C68S mutant). Gαi-DREADD (pcDNA3.1) was used as a synthetic Gαi-coupled GPCR. Briefly, CAL-33 and HET-1A cells were seeded on poly-D-lysine–coated (Sigma-Aldrich, catalog no. P7280), opaque, white 96-well plates (Falcon, catalog no. 353296). The following day, cells were transfected with NanoBiT and receptor plasmids using Lipofectamine 3000 (ThermoFisher Scientific, catalog no. L3000008) according to manufacturer recommendations for a 12-well scale (10 μl of transfection mixture to each well). The NanoBiT plasmids were mixed at a ratio of 100 ng of Gαi1-LgBiT, 500 ng of Gβ1, 500 ng of SmBiT-Gγ2, and 200 ng of receptor if needed. For gene knockdown experiments, 10 pmol of pooled siControl (Dharmacon, catalog no. D-001810-10-20), siFGFR3 (Mission siRNA, catalog no. SIHK0780, SIHK0781, SIHK0782), or siDaple (Dharmacon, catalog no. L-033364-01-0005) was included in the plasmid mixture. The medium was changed the following day. Two days after transfection, media were aspirated from each well and washed once with Hank's buffered salt solution (HBSS). Cells were incubated in HBSS with a final concentration of 5 μM native coelenterazine (Biotium, catalog no. 10110-1) for 30 min at room temperature protected from light. Basal luminescence was read and ligand prepared for final concentrations of 10 ng/ml human basic FGF (bFGF; Roche, catalog no. 11123149001) and 10 μM CNO (Cayman Chemical, catalog no. NC1044836). After ligand addition, luminescence was read in kinetic loops (each well ~every 30 s) for 60 min total (Tecan Spark). Raw luminescent values were normalized to the corresponding basal value for each well and subsequently to the mean vehicle ratio (raw/basal) at time 0. Significance was calculated using a one-way ANOVA at the 60-min time point.

Scratch migration assay

CAL-33 cells were seeded on 12-well plates coated with 10 μg/ml fibronectin in PBS (Sigma-Aldrich, catalog no. F2006-1MG). Once cells reached confluence, a vertical scratch was made with a pipette tip and washed well with PBS before adding serum-free medium. Cells were stimulated with vehicle, 10 ng/ml bFGF, or 1% serum for 24 hours. Images were taken at the 0- and 24-hour time points (2× magnification), and the scratch area was quantified using ImageJ. Percentage scratch closure was calculated for each well and significance was assessed using a one-way ANOVA.

Phosphorylated PAK, ERK, and siRNA knockdown confirmation immunoblots

CAL-33 and HET-1A cells were seeded on poly-D-lysine–coated six-well plates. Cells were transfected with siRNA using Lipofectamine RNAiMAX (Thermo Fisher Scientific, catalog no. 100014472) according to manufacturer recommendations. After overnight serum starvation, cells were stimulated with vehicle, 10 ng/ml bFGF, or 10 μM CNO. Cells were washed once with PBS and lysed in

radioimmunoprecipitation assay (RIPA) buffer (50 mM Tris-HCl, pH 6.8, 150 mM NaCl, 1% NP-40, 0.5% sodium deoxycholate, 0.1% SDS) with protease and phosphatase inhibitors (Bimake, catalog no. B14001, B15001-A/B). Lysates were briefly sonicated and cleared by centrifugation before boiling in Laemmli sample buffer (Bio-Rad catalog no. 1610747). After separation on 10% acrylamide gels and transfer to PVDF membranes, membranes were blocked with 2% BSA in Tris-buffered saline with Tween-20 (TBST) before incubating with antibodies. Primary antibodies against phospho-PAK1(S199/204)/PAK2(S192/197) (1:1000, Cell Signaling Technology, catalog no. 2605), PAK1 (1:2000, Cell Signaling Technology, catalog no. 2602), PAK2 (1:2000, Cell Signaling Technology, catalog no. 2608), pERK (1:2000, Cell Signaling Technology, catalog no. 9106), ERK (1:2000, Cell Signaling Technology, catalog no. 9102), FGFR3 (1:2000, OriGene, catalog no. TA801078), Daple (1:1000, Millipore EMD, catalog no. ABS515), and GAPDH (1:10000, Cell Signaling Technology, catalog no. 2118) were used. After washing with TBST, membranes were incubated in secondary goat anti-rabbit HRP (1:20000, Southern Biotech, catalog no. 4010-05) and goat anti-mouse HRP (1:20000, Southern Biotech, catalog no. 1010-05) antibodies for chemiluminescence development.

CDX3379 treatment: in vivo and in vitro experiments

All the animal studies using HNSCC tumor xenografts were approved by the University of California–San Diego Institutional Animal Care and Use Committee under protocol ASP S15195. All mice were obtained from Charles River Laboratories (Worcester, MA). To establish tumor xenografts, HNSCC cells were transplanted into both flanks (2 million per tumor) of female athymic mice (nu/nu, 4 to 6 weeks of age and weighing 16 to 18 g). Mice were fed with doxycycline food (6 g/kg) from Newco Distributors (Rancho Cucamonga, CA, USA) to induce PIK3CA expression. When average tumor volume reached 100 mm^3, the mice were randomized into groups and treated by intraperitoneal injection with vehicle (PBS) or CDX3379 (10 mg/kg, twice a week) for ~15 days. The mice were sacrificed at the indicated time points (or when mice succumbed to disease, as determined by the ASP guidelines).

Phosphorylated HER3 immunoblots

WT or mutant PIK3CA with FLAG-tag were expressed by lentiviral transduction in SCC-25 cells. Collected cells were washed with ice-cold PBS twice and then lysed with RIPA lysis buffer (150 mM Tris, pH 7.4, 100 mM NaF, 120 mM NaCl, 100 mM sodium orthovanadate) with one tablet of protease inhibitor cocktail (Roche 31075800) and one tablet of phosphatase inhibitor cocktail (Roche 04906837001) added. Lysates (30 μg) were resolved by SDS-PAGE, transferred to PVDF membranes (Bio-Rad, catalog no. 1620177), and incubated with primary antibodies (1:1000) at 4°C overnight. Membranes were then washed and incubated with goat anti-rabbit lgG(H+L)-horseradish peroxidase (HRP)–conjugated secondary antibodies (1:5000) (Bio-Rad, catalog no. 170-6515) for 1 hour at room temperature, followed by washing four times with TBST. Antibodies against P-HER3-Y1197 (catalog no. 4561) and HER3 (catalog no. 12708) were from Cell Signaling Technology, and anti-B-tubulin (catalog no. ab6276) was from Abcam. Blots were quantified with ImageJ software, and the intensity of P-HER3-Y1197 signal was normalized to FLAG-PIK3CA intensity.

IAS background network

The integrated associated stringency (IAS) network was derived from integration of five major types of protein pairwise relationships recorded in public databases: (1) physical PPI, (2) mRNA coexpression, (3) protein coexpression, (4) codependence (correlation of cell line growth upon gene knockouts), and (5) sequence-based relationships. A broad survey created a compendium of 127 network features used as inputs to a random forest regression model, trained to best recover the proximity of protein pairs in the Gene Ontology (GO) resource. The final IAS score, ranging from 0 to 1, quantifies all pairwise associations among 19,035 human proteins. In this study, we displayed stringent protein interactions with IAS > 0.3 when the IAS network was used in figures. More details are described in the companion paper (*76*).

Data analysis

Instant Clue software was used for the generation and statistical analysis of some figures (*84*). Heatmaps were generated with Morpheus (https://software.broadinstitute.org/morpheus).

REFERENCES AND NOTES

1. D. Robinson *et al*., Integrative clinical genomics of advanced prostate cancer. *Cell* **162**, 454 (2015). doi: 10.1016/j.cell.2015.06.053; pmid: 28843286
2. Cancer Genome Atlas Research Network, Comprehensive genomic characterization defines human glioblastoma genes and core pathways. *Nature* **455**, 1061–1068 (2008). doi: 10.1038/nature07385; pmid: 18772890
3. Cancer Genome Atlas Research Network, Integrated genomic analyses of ovarian carcinoma. *Nature* **474**, 609–615 (2011). doi: 10.1038/nature10166; pmid: 21720365
4. Cancer Genome Atlas Network, Comprehensive molecular portraits of human breast tumours. *Nature* **490**, 61–70 (2012). doi: 10.1038/nature11412; pmid: 23000897
5. A. V. Biankin *et al*., Australian Pancreatic Cancer Genome Initiative, Pancreatic cancer genomes reveal aberrations in axon guidance pathway genes. *Nature* **491**, 399–405 (2012). doi: 10.1038/nature11547; pmid: 23103869
6. P. J. Stephens *et al*., Oslo Breast Cancer Consortium (OSBREAC), The landscape of cancer genes and mutational processes in breast cancer. *Nature* **486**, 400–404 (2012). doi: 10.1038/nature11017; pmid: 22722201
7. Cancer Genome Atlas Network, Comprehensive genomic characterization of head and neck squamous cell carcinomas. *Nature* **517**, 576–582 (2015). doi: 10.1038/nature14129; pmid: 25631445
8. K. A. Hoadley *et al*., Cancer Genome Atlas Network,Cell-of-origin patterns dominate the molecular classification of 10,000 tumors from 33 types of cancer. *Cell* **173**, 291–304.e6 (2018). doi: 10.1016/j.cell.2018.03.022; pmid: 29625048
9. M. Hofree, J. P. Shen, H. Carter, A. Gross, T. Ideker, Network-based stratification of tumor mutations. *Nat. Methods* **10**, 1108–1115 (2013). doi: 10.1038/nmeth.2651; pmid: 24037242
10. M. D. M. Leiserson *et al*., Pan-cancer network analysis identifies combinations of rare somatic mutations across pathways and protein complexes. *Nat. Genet.* **47**, 106–114 (2015). doi: 10.1038/ng.3168; pmid: 25501392
11. The Mutation Consequences and Pathway Analysis Working Group of the International Cancer Genome Consortium, Pathway and network analysis of cancer genomes. *Nat. Methods* **12**, 615–621 (2015). doi: 10.1038/nmeth.3440; pmid: 26125594
12. E. Cerami, E. Demir, N. Schultz, B. S. Taylor, C. Sander, Automated network analysis identifies core pathways in glioblastoma. *PLOS ONE* **5**, e8918 (2010). doi: 10.1371/journal.pone.0008918; pmid: 20169195
13. E. O. Paull *et al*., Discovering causal pathways linking genomic events to transcriptional states using Tied Diffusion Through Interacting Events (TieDIE). *Bioinformatics* **29**, 2757–2764 (2013). doi: 10.1093/bioinformatics/btt471; pmid: 23986566
14. T. Li *et al*., A scored human protein-protein interaction network to catalyze genomic interpretation. *Nat. Methods* **14**, 61–64 (2017). doi: 10.1038/nmeth.4083; pmid: 27892958
15. H. Horn *et al*., NetSig: Network-based discovery from cancer genomes. *Nat. Methods* **15**, 61–66 (2018). doi: 10.1038/nmeth.4514; pmid: 29200198
16. Y. Drier, M. Sheffer, E. Domany, Pathway-based personalized analysis of cancer. *Proc. Natl. Acad. Sci. U.S.A.* **110**, 6388–6393 (2013). doi: 10.1073/pnas.1219651110; pmid: 23547110
17. U. D. Akavia *et al*., An integrated approach to uncover drivers of cancer. *Cell* **143**, 1005–1017 (2010). doi: 10.1016/j.cell.2010.11.013; pmid: 21129771
18. M. Paczkowska *et al*., PCAWG Consortium, Integrative pathway enrichment analysis of multivariate omics data. *Nat. Commun.* **11**, 735 (2020). doi: 10.1038/s41467-019-13983-9; pmid: 32024846
19. M. A. Reyna *et al*., PCAWG Consortium, Pathway and network analysis of more than 2500 whole cancer genomes. *Nat. Commun.* **11**, 729 (2020). doi: 10.1038/s41467-020-14367-0; pmid: 32024854
20. T. Rolland *et al*., A proteome-scale map of the human interactome network. *Cell* **159**, 1212–1226 (2014). doi: 10.1016/j.cell.2014.10.050; pmid: 25416956
21. K. Luck *et al*., A reference map of the human binary protein interactome. *Nature* **580**, 402–408 (2020). doi: 10.1038/s41586-020-2188-x; pmid: 32296183
22. E. L. Huttlin *et al*., The BioPlex network: A systematic exploration of the human interactome. *Cell* **162**, 425–440 (2015). doi: 10.1016/j.cell.2015.06.043; pmid: 26186194
23. E. L. Huttlin *et al*., Architecture of the human interactome defines protein communities and disease networks. *Nature* **545**, 505–509 (2017). doi: 10.1038/nature22366; pmid: 28514442
24. M. Y. Hein *et al*., A human interactome in three quantitative dimensions organized by stoichiometries and abundances. *Cell* **163**, 712–723 (2015). doi: 10.1016/j.cell.2015.09.053; pmid: 26496610
25. E. L. Huttlin *et al*., Dual proteome-scale networks reveal cell-specific remodeling of the human interactome. *Cell* **184**, 3022–3040.e28 (2021). doi: 10.1016/j.cell.2021.04.011; pmid: 33961781
26. N. J. Krogan, S. Lippman, D. A. Agard, A. Ashworth, T. Ideker, The cancer cell map initiative: Defining the hallmark networks of cancer. *Mol. Cell* **58**, 690–698 (2015). doi: 10.1016/j.molcel.2015.05.008; pmid: 26000852
27. N. Riaz, L. G. Morris, W. Lee, T. A. Chan, Unraveling the molecular genetics of head and neck cancer through genome-wide approaches. *Genes Dis.* **1**, 75–86 (2014). doi: 10.1016/j.gendis.2014.07.002; pmid: 25642447
28. T. Dogruluk *et al*., Identification of variant-specific functions of PIK3CA by rapid phenotyping of rare mutations. *Cancer Res.* **75**, 5341–5354 (2015). doi: 10.1158/0008-5472.CAN-15-1654; pmid: 26627007
29. M. L. Rudd *et al*., A unique spectrum of somatic PIK3CA (p110alpha) mutations within primary endometrial carcinomas. *Clin. Cancer Res.* **17**, 1331–1340 (2011). doi: 10.1158/1078-0432.CCR-10-0540; pmid: 21266528
30. V. W. Y. Lui *et al*., Frequent mutation of the PI3K pathway in head and neck cancer defines predictive biomarkers. *Cancer*

Discov. **3**, 761–769 (2013). doi: 10.1158/2159-8290.CD-13-0103; pmid: 23619167
31. N. Stransky *et al*., The mutational landscape of head and neck squamous cell carcinoma. *Science* **333**, 1157–1160 (2011). doi: 10.1126/science.1208130; pmid: 21798893
32. D. Martin *et al*., The head and neck cancer cell oncogenome: A platform for the development of precision molecular therapies. *Oncotarget* **5**, 8906–8923 (2014). doi: 10.18632/oncotarget.2417; pmid: 25275298
33. A. A. Molinolo *et al*., Dysregulated molecular networks in head and neck carcinogenesis. *Oral Oncol.* **45**, 324–334 (2009). doi: 10.1016/j.oraloncology.2008.07.011; pmid: 18805044
34. H. Li *et al*., Genomic analysis of head and neck squamous cell carcinoma cell lines and human tumors: A rational approach to preclinical model selection. *Mol. Cancer Res.* **12**, 571–582 (2014). doi: 10.1158/1541-7786.MCR-13-0396; pmid: 24425785
35. K. Yu *et al*., Comprehensive transcriptomic analysis of cell lines as models of primary tumors across 22 tumor types. *Nat. Commun.* **10**, 3574 (2019). doi: 10.1038/s41467-019-11415-2; pmid: 31395879
36. S. Jäger *et al*., Global landscape of HIV-human protein complexes. *Nature* **481**, 365–370 (2011). doi: 10.1038/nature10719; pmid: 22190034
37. G. Teo *et al*., SAINTexpress: Improvements and additional features in Significance Analysis of INTeractome software. *J. Proteomics* **100**, 37–43 (2014). doi: 10.1016/j.jprot.2013.10.023; pmid: 24513533
38. M. E. Sowa, E. J. Bennett, S. P. Gygi, J. W. Harper, Defining the human deubiquitinating enzyme interaction landscape. *Cell* **138**, 389–403 (2009). doi: 10.1016/j.cell.2009.04.042; pmid: 19615732
39. M. Bouhaddou *et al*., Mapping the protein-protein and genetic interactions of cancer to guide precision medicine. *Curr. Opin. Genet. Dev.* **54**, 110–117 (2019). doi: 10.1016/j.gde.2019.04.005; pmid: 31288129
40. M. Eckhardt *et al*., Multiple routes to oncogenesis are promoted by the human papillomavirus-host protein network. *Cancer Discov.* **8**, 1474–1489 (2018). doi: 10.1158/2159-8290.CD-17-1018; pmid: 30209081
41. S. Pyndiah *et al*., c-MYC suppresses BIN1 to release poly(ADP-ribose) polymerase 1: A mechanism by which cancer cells acquire cisplatin resistance. *Sci. Signal.* **4**, ra19 (2011). doi: 10.1126/scisignal.2001556; pmid: 21447800
42. M. Kalkat *et al*., MYC protein interactome profiling reveals functionally distinct regions that cooperate to drive tumorigenesis. *Mol. Cell* **72**, 836–848.e7 (2018). doi: 10.1016/j.molcel.2018.09.031; pmid: 30415952
43. A. Czubaty *et al*., Proteomic analysis of complexes formed by human topoisomerase I. *Biochim. Biophys. Acta* **1749**, 133–141 (2005). doi: 10.1016/j.bbapap.2005.03.007; pmid: 15848144
44. K. Haraguchi *et al*., Ajuba negatively regulates the Wnt signaling pathway by promoting GSK-3beta-mediated phosphorylation of beta-catenin. *Oncogene* **27**, 274–284 (2008). doi: 10.1038/sj.onc.1210644; pmid: 17621269
45. Y. Feng, G. D. Longmore, The LIM protein Ajuba influences interleukin-1-induced NF-kappaB activation by affecting the assembly and activity of the protein kinase Czeta/p62/TRAF6 signaling complex. *Mol. Cell. Biol.* **25**, 4010–4022 (2005). doi: 10.1128/MCB.25.10.4010-4022.2005; pmid: 15870274
46. W. Fan *et al*., Keap1 facilitates p62-mediated ubiquitin aggregate clearance via autophagy. *Autophagy* **6**, 614–621 (2010). doi: 10.4161/auto.6.5.12189; pmid: 20495340
47. A. Lau *et al*., A noncanonical mechanism of Nrf2 activation by autophagy deficiency: Direct interaction between Keap1 and p62. *Mol. Cell. Biol.* **30**, 3275–3285 (2010). doi: 10.1128/MCB.00248-10; pmid: 20421418
48. I. M. Copple *et al*., Physical and functional interaction of sequestosome 1 with Keap1 regulates the Keap1-Nrf2 cell defense pathway. *J. Biol. Chem.* **285**, 16782–16788 (2010). doi: 10.1074/jbc.M109.096545; pmid: 20378532
49. E. Hamilton, J. R. Infante, Targeting CDK4/6 in patients with cancer. *Cancer Treat. Rev.* **45**, 129–138 (2016). doi: 10.1016/j.ctrv.2016.03.002; pmid: 27017286
50. N. P. Fusté *et al*., Characterization of cytoplasmic cyclin D1 as a marker of invasiveness in cancer. *Oncotarget* **7**, 26979–26991 (2016). doi: 10.18632/oncotarget.8876; pmid: 27105504
51. A. Oshita *et al*., Identification and characterization of a novel Dvl-binding protein that suppresses Wnt signalling pathway. *Genes Cells* **8**, 1005–1017 (2003). doi: 10.1111/j.1365-2443.2003.00692.x; pmid: 14750955
52. N. Aznar *et al*., Convergence of Wnt, growth factor, and heterotrimeric G protein signals on the guanine nucleotide exchange factor Daple. *Sci. Signal.* **11**, eaao4220 (2018). doi: 10.1126/scisignal.aao4220; pmid: 29487190
53. N. Aznar *et al*., A Daple-Akt feed-forward loop enhances noncanonical Wnt signals by compartmentalizing β-catenin. *Mol. Biol. Cell* **28**, 3709–3723 (2017). doi: 10.1091/mbc.e17-06-0405; pmid: 29021338
54. M. Ishida-Takagishi *et al*., The Dishevelled-associating protein Daple controls the non-canonical Wnt/Rac pathway and cell motility. *Nat. Commun.* **3**, 859 (2012). doi: 10.1038/ncomms1861; pmid: 22643886
55. N. Aznar *et al*., Daple is a novel non-receptor GEF required for trimeric G protein activation in Wnt signaling. *eLife* **4**, e07091 (2015). doi: 10.7554/eLife.07091; pmid: 26126266
56. J. Park *et al*., Association of p21-activated kinase-1 activity with aggressive tumor behavior and poor prognosis of head and neck cancer. *Head Neck* **37**, 953–963 (2015). doi: 10.1002/hed.23695; pmid: 24634274
57. A. Tsherniak *et al*., Defining a cancer dependency map. *Cell* **170**, 564–576.e16 (2017). doi: 10.1016/j.cell.2017.06.010; pmid: 28753430
58. G. L. Dornan, J. E. Burke, Molecular mechanisms of human disease mediated by oncogenic and primary immunodeficiency mutations in class IA phosphoinositide 3-kinases. *Front. Immunol.* **9**, 575 (2018). doi: 10.3389/fimmu.2018.00575; pmid: 29616047
59. Z. Songyang *et al*., Specific motifs recognized by the SH2 domains of Csk, 3BP2, fps/fes, GRB-2, HCP, SHC, Syk, and Vav. *Mol. Cell. Biol.* **14**, 2777–2785 (1994). doi: 10.1128/MCB.14.4.2777; pmid: 7511210
60. L. Zhao, P. K. Vogt, Helical domain and kinase domain mutations in p110 of phosphatidylinositol 3-kinase induce gain of function by different mechanisms. *Proc. Natl. Acad. Sci. U.S.A.* **105**, 2652–2657 (2008). doi: 10.1073/pnas.0712169105; pmid: 18268322
61. B. Alberts, The cell as a collection of protein machines: Preparing the next generation of molecular biologists. *Cell* **92**, 291–294 (1998). doi: 10.1016/S0092-8674(00)80922-8; pmid: 9476889
62. D. Hanahan, R. A. Weinberg, The hallmarks of cancer. *Cell* **100**, 57–70 (2000). doi: 10.1016/S0092-8674(00)81683-9; pmid: 10647931
63. M. Kim *et al*., A protein interaction landscape of breast cancer. *Science* **374**, eabf3066 (2021).
64. D. Salas, R. G. Stacey, M. Akinlaja, L. J. Foster, Next-generation interactomics: Considerations for the use of co-elution to measure protein interaction networks. *Mol. Cell. Proteomics* **19**, 1–10 (2020). doi: 10.1074/mcp.R119.001803; pmid: 31792070
65. B. T. Lobingier *et al*., An approach to spatiotemporally resolve protein interaction networks in living cells. *Cell* **169**, 350–360.e12 (2017). doi: 10.1016/j.cell.2017.03.022; pmid: 28388416
66. P. Samavarchi-Tehrani, R. Samson, A.-C. Gingras, Proximity dependent biotinylation: Key enzymes and adaptation to proteomics approaches. *Mol. Cell. Proteomics* **19**, 757–773 (2020). doi: 10.1074/mcp.R120.001941; pmid: 32127388
67. O. Klykov *et al*., Efficient and robust proteome-wide approaches for cross-linking mass spectrometry. *Nat. Protoc.* **13**, 2964–2990 (2018). doi: 10.1038/s41596-018-0074-x; pmid: 30446747
68. M. Parvathy, S. Sreeja, R. Kumar, M. R. Pillai, Potential role of p21 activated kinase 1 (PAK1) in the invasion and motility of oral cancer cells. *BMC Cancer* **16**, 293 (2016). doi: 10.1186/s12885-016-2263-8; pmid: 27229476
69. M. Schuler *et al*., Rogaratinib in patients with advanced cancers selected by FGFR mRNA expression: A phase 1 dose-escalation and dose-expansion study. *Lancet Oncol.* **20**, 1454–1466 (2019). doi: 10.1016/S1470-2045(19)30412-7; pmid: 31405822
70. E. I. Dumbrava, R. Alfattal, V. A. Miller, A. M. Tsimberidou, Complete response to a fibroblast growth factor receptor inhibitor in a patient with head and neck squamous cell carcinoma harboring FGF amplifications. *JCO Precis. Oncol.* **2**, 1–7 (2018). doi: 10.1200/PO.18.00100; pmid: 31123723
71. J. D. Carson *et al*., Effects of oncogenic p110alpha subunit mutations on the lipid kinase activity of phosphoinositide 3-kinase. *Biochem. J.* **409**, 519–524 (2008). doi: 10.1042/BJ20070681; pmid: 17877460
72. U. Duvvuri *et al*., Molecular and clinical activity of CDX-3379, an anti-ErbB3 monoclonal antibody, in head and neck squamous cell carcinoma patients. *Clin. Cancer Res.* **25**, 5752–5758 (2019). doi: 10.1158/1078-0432.CCR-18-3453; pmid: 31308059
73. S. Lee *et al*., Inhibition of ErbB3 by a monoclonal antibody that locks the extracellular domain in an inactive configuration. *Proc. Natl. Acad. Sci. U.S.A.* **112**, 13225–13230 (2015). doi: 10.1073/pnas.1518361112; pmid: 26460020
74. D. Alvarado *et al*., ErbB activation signatures as potential biomarkers for anti-ErbB3 treatment in HNSCC. *PLOS ONE* **12**, e0181356 (2017). doi: 10.1371/journal.pone.0181356; pmid: 28723928
75. F. Janku, T. A. Yap, F. Meric-Bernstam, Targeting the PI3K pathway in cancer: Are we making headway? *Nat. Rev. Clin. Oncol.* **15**, 273–291 (2018). doi: 10.1038/nrclinonc.2018.28; pmid: 29508857
76. F. Zheng *et al*., Convergence of cancer mutation on a hierarchy of protein systems. *Science* **374**, eabf3067 (2021).
77. M. Uhlen *et al*., A pathology atlas of the human cancer transcriptome. *Science* **357**, eaan2507 (2017). doi: 10.1126/science.aan2507; pmid: 28818916
78. J. Cox, M. Mann, MaxQuant enables high peptide identification rates, individualized p.p.b.-range mass accuracies and proteome-wide protein quantification. *Nat. Biotechnol.* **26**, 1367–1372 (2008). doi: 10.1038/nbt.1511; pmid: 19029910
79. M. Choi *et al*., MSstats: An R package for statistical analysis of quantitative mass spectrometry-based proteomic experiments. *Bioinformatics* **30**, 2524–2526 (2014). doi: 10.1093/bioinformatics/btu305; pmid: 24794931
80. J. A. Vizcaíno *et al*., ProteomeXchange provides globally coordinated proteomics data submission and dissemination. *Nat. Biotechnol.* **32**, 223–226 (2014). doi: 10.1038/nbt.2839; pmid: 24727771
81. Y. Perez-Riverol *et al*., The PRIDE database and related tools and resources in 2019: Improving support for quantification data. *Nucleic Acids Res.* **47**, D442–D450 (2019). doi: 10.1093/nar/gky1106; pmid: 30395289
82. B. MacLean *et al*., Skyline: An open source document editor for creating and analyzing targeted proteomics experiments. *Bioinformatics* **26**, 966–968 (2010). doi: 10.1093/bioinformatics/btq054; pmid: 20147306
83. A. Inoue *et al*., Illuminating G-protein-coupling selectivity of GPCRs. *Cell* **177**, 1933–1947.e25 (2019). doi: 10.1016/j.cell.2019.04.044; pmid: 31160049
84. H. Nolte, T. D. MacVicar, F. Tellkamp, M. Krüger, Instant Clue: A software suite for interactive data visualization and analysis. *Sci. Rep.* **8**, 12648 (2018). doi: 10.1038/s41598-018-31154-6; pmid: 30140043
85. S. Orchard *et al*., Protein interaction data curation: The International Molecular Exchange (IMEx) consortium. *Nat. Methods* **9**, 345–350 (2012). doi: 10.1038/nmeth.1931; pmid: 22453911
86. R. Oughtred *et al*., The BioGRID database: A comprehensive biomedical resource of curated protein, genetic, and chemical interactions. *Protein Sci.* **30**, 187–200 (2021). doi: 10.1002/pro.3978; pmid: 33070389
87. M. Giurgiu *et al*., CORUM: The comprehensive resource of mammalian protein complexes-2019. *Nucleic Acids Res.* **47**, D559–D563 (2019). doi: 10.1093/nar/gky973; pmid: 30357367
88. D. Chakravarty *et al*., A precision oncology knowledge base. *JCO Precis. Oncol.* **1**, 1–16 (2017). doi: 10.1200/PO.17.00011; pmid: 28890946
89. Y. Zhao *et al*., Crystal structures of PI3Kα complexed with PI103 and its derivatives: New directions for inhibitors design. *ACS Med. Chem. Lett.* **5**, 138–142 (2013). doi: 10.1021/ml400378e; pmid: 24900786
90. J. Gao *et al*., Integrative analysis of complex cancer genomics and clinical profiles using the cBioPortal. *Sci. Signal.* **6**, pl1 (2013). doi: 10.1126/scisignal.2004088; pmid: 23550210
91. Protein interaction network for: D. L. Swaney *et al*., A protein network map of head and neck cancer reveals PIK3CA mutant drug sensitivity, NEDx (2021); https://doi.org/10.18119/N9R010.

ACKNOWLEDGMENTS

Funding: This work was supported by the National Institutes of Health (NIH grant U54 CA209891 to J.R.G., J.S.G., T.I., and N.J.K.); a George and Judy Marcus Award in Precision Medicine Innovation (to J.R.G. and N.J.K.); NIH grant R35CA231998 and an American Cancer Society Clinical Research Professorship to J.R.G.; NIH grant R01DE028289 to J.R.G. and D.E.J.; NIH grants R01DE026644, R01DE026870, and R01CA247551 to J.S.G.; NIH grants U24 CA184427 and P41 GM103504 to T.I.; NIH grant R50 CA243885 to J.F.K.; NIH grant R01 GM109176 to N.Ju.; NIH grant F32CA239333 to M.B.; and the Martha and Bruce Atwater Breast Cancer Research Program, the UCSF Prostate Cancer Program, and the Benioff Initiative for Prostate Cancer Research (to M.K.). Data for this study were acquired at the Center for Advanced Light Microscopy- Nikon Imaging Center at UCSF on instruments

obtained using grants from the UCSF Program for Breakthrough Biomedical Research funded in part by the Sandler Foundation and the UCSF Research Resource Fund Award. **Author contributions:** Project conception by N.J.K., T.I., and D.L.S.; cloning by K.K. and M.S.; cell culture by N.B., R.O., M.S., and H.F.; AP-MS purifications by M.S.; data analysis by J.P., D.L.S., J.V.D., D.J.-M., and M.B.; differential interaction scoring by J.P.; IAS network generation by F.Z.; FGFR3:Daple validation experiments by D.J.R.; HER3 activity Western blots by Y.Z.; co-IP Western blotting by N.Ji. and N.K.V.; in vivo mouse experiments by Z.W. and Y.G.; structural analysis by N.Ju.; proximity ligation assays by H.F., M.M., and K.A.H.; manuscript preparation by D.E.J., J.R.G., T.I., J.P., N.Ju., M.K., K.O., R.O., D.L.S., and N.J.K.; supervision by D.E.J., J.R.G., J.S.G., T.I., J.F.K., D.L.S., and N.J.K. **Competing interests:** J.S.G. is a member of the Board of Scientific Advisors for Vividion, Oncoceutics Pharmaceuticals, and Domain Pharmaceuticals. T.I. is the cofounder of Data4Cure Inc. with an equity interest and has a funded sponsored research agreement from Ideaya BioSciences Inc. with an equity stake. The laboratory of N.J.K. has received research support from Vir Biotechnology and F. Hoffmann-La Roche. N.J.K. has consulting agreements with the Icahn School of Medicine at Mount Sinai, New York, Maze Therapeutics, and Interline Therapeutics; is a shareholder of Tenaya Therapeutics; and has received stocks from Maze Therapeutics and Interline Therapeutics. N.Ju. is a member of the Science Advisory Board of Turning Point Therapeutics, SUDO Biosciences, and Type6 Therapeutics; a shareholder of Turning Point Therapeutics; and a stock option holder of SUDO Biosciences and Type6 Therapeutics. **Data and materials availability:** Further information and requests for resources and reagents should be directed and will be fulfilled by N.J.K. All raw MS data files and search results are available from the Pride partner ProteomeXchange repository under the PXD019469 identifier, and the PPI network is viewable on NEDx (*91*).

SUPPLEMENTARY MATERIALS

https://science.org/doi/10.1126/science.abf2911
Figs. S1 to S6
Data S1 to S7
MDAR Reproducibility Checklist

View/request a protocol for this paper from *Bio-protocol*.

17 October 2020; accepted 28 July 2021
10.1126/science.abf2911

Science

A protein network map of head and neck cancer reveals PIK3CA mutant drug sensitivity

Danielle L. SwaneyDana J. RammsZhiyong WangJisoo ParkYusuke GotoMargaret SoucherayNeil BholaKyumin KimFan ZhengYan ZengMichael McGregorKari A. HerringtonRachel O'KeefeNan JinNathan K. VanLandinghamHelene FoussardJohn Von DollenMehdi BouhaddouDavid Jimenez-MoralesKirsten ObernierJason F. KreisbergMinkyu KimDaniel E. JohnsonNatalia JuraJennifer R. GrandisJ. Silvio GutkindTrey IdekerNevan J. Krogan

Science, 374 (6563), eabf2911. • DOI: 10.1126/science.abf2911

Mapping protein interactions driving cancer

Cancer is a genetic disease, and much cancer research is focused on identifying carcinogenic mutations and determining how they relate to disease progression. Three papers demonstrate how mutations are processed through networks of protein interactions to promote cancer (see the Perspective by Cheng and Jackson). Swaney *et al*. focus on head and neck cancer and identify cancer-enriched interactions, demonstrating how point mutant–dependent interactions of PIK3CA, a kinase frequently mutated in human cancers, are predictive of drug response. Kim *et al*. focus on breast cancer and identify two proteins functionally connected to the tumor-suppressor gene BRCA1 and two proteins that regulate PIK3CA. Zheng *et al*. developed a statistical model that identifies protein networks that are under mutation pressure across different cancer types, including a complex bringing together PIK3CA with actomyosin proteins. These papers provide a resource that will be helpful in interpreting cancer genomic data. —VV

Science (ISSN) is published by the American Association for the Advancement of Science. 1200 New York Avenue NW, Washington, DC 20005. The title *Science* is a registered trademark of AAAS.